

Robust Identification of Active Galactic Nuclei through *HST* Optical Variability in GOODS-S: Comparison with the X-ray and mid-IR Selected Samples

E. Pouliaxis^{1,2*}, I. Georgantopoulos¹, A. Z. Bonanos¹, M. Yang¹, K. V. Sokolovsky^{3,4,1}, D. Hatzidimitriou^{2,1}, G. Mountrichas¹, P. Gavras^{5,1}, V. Charmandaris^{6,7}, I. Bellas-Velidis¹, Z. T. Spetsieri^{1,2} and K. Tsinganos^{2,1}

¹IAASARS, National Observatory of Athens, 15236 Penteli, Greece

²Department of Astrophysics, Astronomy & Mechanics, Faculty of Physics, University of Athens, Zografos, 15783 Athens, Greece

³Sternberg Astronomical Institute, Moscow State University, Universitetskii pr. 13, 119992 Moscow, Russia

⁴Astro Space Center of Lebedev Physical Institute, Profsoyuznaya Str. 84/32, 117997 Moscow, Russia

⁵Rhea for ESA/ESAC, Camino bajo del Castillo, s/n, Urbanizacion Villafranca del Castillo, Villanueva de la Cañada, 28692 Madrid, Spain

⁶University of Crete, Department of Physics, GR-71003 Heraklion, Greece

⁷Institute of Astrophysics, Foundation for Research and Techno-Hellas, GR-71110 Heraklion, Greece

Accepted 2019 May 27. Received 2019 May 24; in original form 2019 February 15

ABSTRACT

Identifying Active Galactic Nuclei (AGNs) through their X-ray emission is efficient, but necessarily biased against X-ray-faint objects. We aim to characterize this bias by comparing X-ray-selected AGNs to the ones identified through optical variability and mid-IR colours. We present a catalogue of AGNs selected through optical variability using all publicly available z-band *Hubble* Space Telescope images in the GOODS-South field. For all objects in the catalogue, we compute X-ray upper limits or discuss detections in the deepest available ~ 7 Ms *Chandra* Deep Field South images and present the *Spitzer*/IRAC mid-IR colours. For the variability study, we consider only sources observed over at least five epochs and over a time baseline of up to ten years. We adopt the elevated median absolute deviation as a variability indicator robust against individual outlier measurements and identify 113 variability-selected AGN candidates. Among these, 26 have an X-ray counterpart and lie within the conventional AGN area in the F_X/F_{opt} diagram. The candidates with X-ray upper limits are on average optically fainter, have higher redshifts compared to the X-ray detected ones and are consistent with low luminosity AGNs. Out of 41 variable optical sources with IR detections, 13 fulfill the IR AGN colour selection criteria. Our work emphasizes the importance of optical variability surveys for constructing complete samples of AGNs including the ones that remain undetected even by the deepest X-ray and IR surveys.

Key words: galaxies: active – galaxies: photometry – galaxies: nuclei – x-rays: galaxies – methods: observational

1 INTRODUCTION

It is widely accepted that massive galaxies and a fraction of lower mass galaxies host a supermassive black hole in their centre (Magorrian et al. 1998; Kormendy & Kennicutt 2004; Filippenko & Ho 2003; Barth et al. 2004; Greene & Ho 2004, 2007; Dong et al. 2007; Greene et al. 2008). More-

over, there is a correlation between the mass of the black holes and the properties of their host galaxies (Kormendy & Ho 2013), such as the luminosity, the stellar mass, the velocity dispersion or the bulge rotational velocity (Dressler 1989; Kormendy & Richstone 1995; Magorrian et al. 1998; Ferrarese & Merritt 2000; Gebhardt et al. 2000; Tremaine et al. 2002; Marconi & Hunt 2003; Häring & Rix 2004; Ferrarese & Ford 2005; Graham & Driver 2007; Gültekin et al. 2009). Hence, either the processes that take place in Active

* E-mail: epouliaxis@astro.noa.gr

Galactic Nuclei (AGNs) play an important role in star formation and shaping of the galaxy structure, or vice versa the galaxy evolution directly affects the mass and spin of the central black hole. To better understand the relations between the central black hole and its host galaxy, it is necessary to have complete samples of AGNs, not biased against redshift, obscuration, luminosity, etc.

X-rays penetrate deep into material with high column densities and therefore are nearly unaffected by moderate obscuration ($N_H < 10^{24} \text{ cm}^{-2}$) (Brandt & Alexander 2015; Alexander 2017). Thus wide-field X-ray imaging constitutes the most common and efficient technique to identify AGN. Other methods make use of infrared (IR), ultraviolet and optical single and multiple colour selection criteria to identify AGNs, as the AGN spectral energy distributions differ from those of normal galaxies or stars (Richards et al. 2002, 2005; Lacy et al. 2004; Stern et al. 2005; Alonso-Herrero et al. 2006; Donley et al. 2007; Schneider et al. 2007, 2010). However, at these wavelengths, the AGN samples may be contaminated by foreground stars or biased by the dust emission from the host galaxies compared to X-ray AGN identification where the dilution by the hosts is not that dominant.

An alternative method to identify AGNs is based on the detection of variability at any wavelengths on timescales from hours to years (Ulrich et al. 1997; Kawaguchi et al. 1998; Paolillo et al. 2004; García-González et al. 2014). There is a correlation between the amplitude of the AGN variability and the timescale of variation (Hook et al. 1994; Trevese et al. 1994; Cristiani et al. 1997; di Clemente et al. 1996; Vanden Berk et al. 2004; Kelly et al. 2009; Bauer et al. 2009; Middei et al. 2017), the redshift and the black hole mass (for timescales longer than 100 days; Cristiani et al. 1990; Hook et al. 1994; Trevese et al. 1994; Vanden Berk et al. 2004). On the other hand, the variability amplitude is anticorrelated with the rest-frame wavelength (di Clemente et al. 1996; Cristiani et al. 1997; Giveon et al. 1999; Helfand et al. 2001; Vanden Berk et al. 2004; Zuo et al. 2012) and the nuclear luminosity (Trevese et al. 1994; Vagnetti et al. 2016). The latter suggests that low-luminosity AGNs (LLAGNs) will dominate a variability survey compared to more luminous AGNs.

Several theories and mechanisms have been proposed to explain the variability. For example, Rees (1984) and Kawaguchi et al. (1998) proposed that AGN variability may be due to the fact that accretion disks are vulnerable to dynamical instabilities, while Li & Cao (2008) and Zuo et al. (2012) attributed the variability to fluctuations in the accretion rate. In the extreme case of blazars (the most luminous class of AGNs possessing a relativistic jet pointing towards the observer), the variability is modulated by changes in the accretion disk, but also by non-thermal power-law emission from the jets and the (not fully explored) connection between them (Gu & Li 2013; Finke & Becker 2014; Chatterjee et al. 2018). Other interpretations of AGN variability include gravitational microlensing effects (Hawkins 1993; Alexander 1995), tidal disruption events (Komossa 2015) and multiple explosions of supernovae (SNe) near the nuclei (Kawaguchi et al. 1998; Terlevich et al. 1992).

In the last several years, AGN variability has been used in many studies. In the X-ray region, Young et al. (2012) and Ding et al. (2018) selected LLAGNs in the 4 and 7 Ms *Chandra* Deep Field South (CDF-S), respectively. In the

optical and near IR bands, Sarajedini et al. (2003, 2011); Trevese et al. (2008); Villforth et al. (2010); Simm et al. (2015); Falocco et al. (2015); Graham et al. (2014); De Cicco et al. (2015); Baldassare et al. (2018); Kim et al. (2018) identified a large sample of AGNs, suggesting that the search for variability at short time scales is efficient in selecting LLAGNs that would have been missed by X-ray surveys. As AGNs exhibit a red-noise behaviour (Lawrence & Papadakis 1993; Park & Trippe 2017; i.e. they have more power at low frequencies in the Fourier space), De Cicco et al. (2015) and Paolillo et al. (2017) pointed out that the longer the time baseline (e.g. greater than few years), the larger the variability amplitude and the more complete is the AGN selection.

However, while blazars tend to show variability at all timescales, the power spectrum and structure function analysis of light curves of many radio-quiet AGNs suggest that their variability amplitude does not rise indefinitely with longer timescales. Their power spectrum flattens below some frequency. Such power spectra were modeled with a damped random walk and continuous auto-regressive moving average models (de Vries et al. 2005; Kelly et al. 2009; MacLeod et al. 2010; MacLeod et al. 2012; Kelly et al. 2014; Kasliwal et al. 2015; Kozłowski 2016; Simm et al. 2016).

In order to study AGN variability over cosmic time one needs a deep field observed multiple times. The Great Observatories Origins Deep Survey Southern field (GOODS-S Giavalisco et al. 2004) centered at $\alpha = 3\text{h}32\text{m}30\text{s}$ $\delta = -27^\circ 48' 20''$ J2000, covers an area of $10' \times 16'$. It is the most data-rich area of the sky in terms of depth and wavelength coverage and as it has been observed by the *Hubble* Space Telescope (HST) multiple times, it perfectly satisfies the requirements of our study.

Variability studies in this field based on HST multi-epoch data have been performed by Sarajedini et al. (2011) and Villforth et al. (2010, 2012). Sarajedini et al. (2011) used the *V*-band (F606W) images over five epochs spanning almost seven months and the standard deviation, σ , as the statistical variability indicator to identify 42 variable sources. The authors compared their results with the mid-IR and the 2Ms *Chandra* X-ray data. Villforth et al. (2010) identified 88 variable sources (out of $\sim 6,000$ sources) using the C-statistic (the ratio of the measured standard deviation, σ , to the expected one σ_{exp} , in this case scaled from the estimated photometric errors; de Diego 2010) on *z*-band data with the same epochs and time baseline as in Sarajedini et al. (2011). The authors, after removing the false positive detections and the stellar population, validated the AGN nature of 55/88 variable sources through spectral energy distribution fitting, the identification of X-ray counterparts in the CDF-S 4Ms catalogue and auxiliary radio and IR data (Villforth et al. 2012).

The field was also targeted in ground-based optical variability studies. Trevese et al. (2008) studied the variability of sources in AXAF, a larger field that includes GOODS-S. They analysed *V*-band images taken from ground-based telescopes and used magnitude differences between eight epochs over two years of observations to identify 132 variable AGN candidates. Similarly, Falocco et al. (2015) applied a multi-epoch variability search spanning six months with the SUDARE-VOICE survey dataset obtained with the VLT Survey Telescope. They selected 175 variable sources

over an area of 2 deg^2 around CDF-S using σ as the variability index. They compared the optical variable sample with AGNs selected through optical-NIR and IR colour diagnostics and AGNs with X-ray counterparts in the 4Ms CDF-S catalogue.

We extend the previous HST-based studies of Sarajedini et al. (2011) and Villforth et al. (2010, 2012) by using the latest data, variability detection and IR-colour-based AGN selection techniques. We construct a new catalogue of optically variable AGNs based on HST z -band observations and comparing it with other selection techniques. We highlight the following novel aspects of this study:

- We expand the time baseline of the deep HST observations of GOODS-S up to ten years, which should result in a more complete AGN selection.
- We use the Median Absolute Deviation (MAD) as the variability-detection statistic, which, unlike σ , is robust against individual outlier measurements (Sokolovsky et al. 2017b). We expect MAD to yield a cleaner sample of variable sources compared to the previous studies.
- We use the new deepest available 7Ms *Chandra* image to constrain the X-ray brightness of the variability-selected AGNs.
- We compare our variable sample with AGN selected in the mid-IR using the Lacy et al. (2007) and Donley et al. (2012) criteria.

The HST optical observations and the data reduction (astrometry and photometry) along with ancillary data used in this work are presented in Section 2, while in Section 3, we describe the method we used to create the list of variable sources. We also exclude stars and supernovae from the sample of the AGN candidates. In Section 4, we demonstrate the properties of the AGN candidates (e.g. magnitude and redshift distributions or X-ray luminosities) and construct the mid-IR AGN samples. In Section 5, we compare our results with other variability studies and we discuss the differences between optically variable, mid-IR and X-ray selected AGNs, while Section 6 presents the summary of the results and conclusions.

2 DATA REDUCTION

2.1 Optical HST data

We analyze all publicly available images of the GOODS-S region obtained with the Wide Field Channel of the HST Advanced Camera for Surveys (ACS, Ford et al. 1998) in the F850LP filter (z -band). The images are collected from the Hubble *Legacy Archive (HLA) Data Release 10*¹. Each image corresponds to an individual HST visit and results from a combination of three or more individual exposures with the purpose of rejecting the cosmic rays. The observations were collected in the framework of the observing programs listed in Table 1. We analyze totally 437 individual images spanning up to 10 years in some regions.

We used the code developed by M. Tewes² which is based on P. G. van Dokkum’s L.A.Cosmic algorithm (van

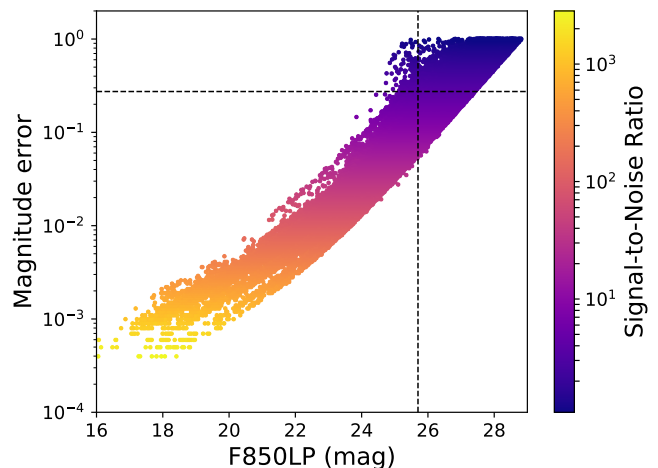


Figure 1. The magnitude errors as a function of the magnitude for each detection. The measurements are colour coded by the SNR. The vertical and horizontal lines represent the limits in magnitude and magnitude error, respectively, after the SNR filtering.

Dokkum 2001) to further reduce the cosmic-ray contamination of the visit-combined images, especially on the edges of the combined frames. This algorithm is based on variations of the Laplacian edge detection and is capable of rejecting any cosmic ray, regardless of its shape and size, keeping at the same time the faint point-like sources untouched.

Source detection and photometry was performed using SExtractor (Bertin & Arnouts 1996, 2010). We applied the *mexican hat* spatial filter for detection and set the minimum contrast parameter for deblending (`deblend_mincont`) to 0.0075 in order to avoid multiple detections for individual extended sources. This did not affect the unresolved sources, since the GOODS-S field is not crowded. For the photometry and the variability analysis, we used a circular aperture with a radius of $0.36''$. This was the radius used by Villforth et al. (2010) as for smaller radii the photometry is affected by changes in the point-spread function and aperture centring issues. In addition, we measured the magnitudes for two more radii ($0.05''$ and $0.15''$), which correspond to the ones used for the *Hubble* Source Catalogue (HSC, Whitmore et al. 2016) apertures (`MagAper1` and `MagAper2`). The latter were used to compute the concentration index (CI) and to validate our photometry against the HSC. CI is an indicator of the extension of a source and is described below.

After visually inspecting images associated with outlier points appearing in many light curves, we noticed that many outliers were situated near the frame edge or the gap between CCD chips in these images. This is related to the background estimation, which is essential for aperture photometry. Because the images have been resampled to a north-up east-left orientation, blank areas appear around the actual image (e.g. CCD gaps and image edges). SExtractor uses these blank areas and gets incorrect background estimates. To avoid this effect and, consequently, outliers and false-positive variable sources, we used the weight images provided by HLA and excluded all detections located within 10 pixels, or $\sim 0.5''$, from the edges ($\sim 1\%$ of all the detections).

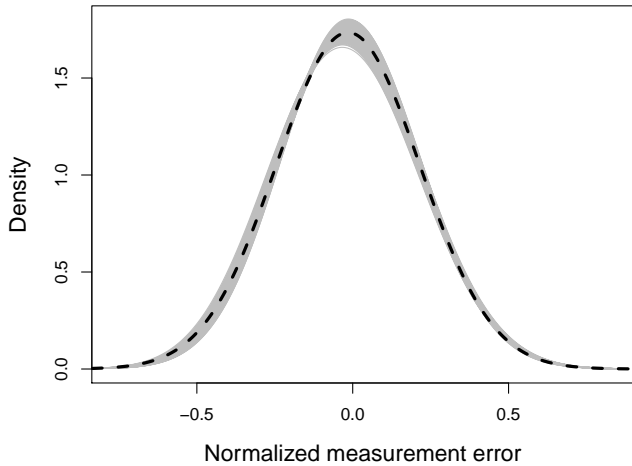
To ensure the quality of the data but also enable the

¹ <http://hla.stsci.edu/>

² http://obswww.unige.ch/~tewes/cosmics_dot_py/

Table 1. The HST Treasury programs included in this study

Prop. ID	PI Name	Cycle	$N_{\text{img}}^{\text{a}}$	$N_{\text{exp}}^{\text{b}}$	Exp. Time (s)	Start_Obs ^c	End_Obs ^c
9352	A. Riess	11	12	4	1880-4800	2002-10	2003-02
9425	M. Giavalisco	11	78	4	2040-2120	2003-02	2003-02
9488	K. Ratnatunga	11	2	3	1800	2002-09	2003-02
9500	H-W. Rix	11	58	3	2160-2286	2002-09	2003-02
9803	R. Thompson	12	18	6	6900	2003-08	2003-11
9978	S. Beckwith	12	68	4	4660-4860	2003-09	2004-01
10086	S. Beckwith	12	3	4	4660	2003-12	2003-12
10189	A. Riess	13	23	3-4	1200-2000	2004-09	2005-01
10258	C. Kretchmer	13	20	4	3034	2004-10	2006-09
10340	A. Riess	13	75	4	1440-1600	2004-07	2005-02
11144	R. Bouwens	16	1	4	2046	2009-10	2009-10
11563	G. Illingworth	17	31	4	5102-5332	2009-08	2010-08
12060	S. Faber	18	15	4	2046-2330	2011-03	2011-11
12061	S. Faber	18	11	5	1836-2086	2010-11	2011-06
12062	S. Faber	18	15	5	1886-1986	2011-07	2011-12
12099	A. Riess	18	4	4-5	1886-2070	2010-12	2011-08
12461	A. Riess	19	2	4	1943-1992	2012-02	2012-03
12534	H. Teplitz	19	1	4	5000	2012-05	2012-05

Note. – (a): Number of combined (level 2) images. (b): Number of single exposure images. (c): Starting and ending time of the observations.**Figure 2.** The distributions of the normalized measurement errors for each magnitude bin (gray). The black dashed line represent the Gaussian fit to the data. The units are given in magnitudes.

search for small amplitude variations, we selected measurements with a signal-to-noise ratio (SNR) greater than five. The SNR was calculated for each of the detections for all images using the fluxes and the corresponding flux errors derived with SExtractor. In Figure 1, we plot the magnitude error as a function of the magnitude, colour-coded with SNR. The relation between magnitude and magnitude error is approximately linear as expected if the errors are mainly statistical at the faint end. After applying the SNR cut-off, the faintest sources have an average error of about 0.25 mag.

We also divided all the detections into magnitude bins and over-plotted the distributions of the normalized magnitude errors (after subtracting the median) for each of the magnitude bins in order to check if all detections of the same

magnitude have similar errors. Figure 2 shows that these distributions are approximately Gaussian. The distribution would have been skewed, if there was a group of sources measured with systematically larger uncertainties (e.g. due to bright local background).

Since the astrometric accuracy of the HST is limited by the positional accuracy of individual Guide Star Catalogue stars (Lasker et al. 2008), we applied a triangle matching technique based on the Valdes et al. (1995) algorithm to find the astrometric solution. We used the `match_v1` program by M. W. Richmond³ to automatically determine the coordinate system corrections using the 50 brightest sources in each source list. We used the second version of HSC (HSCv2) as the reference catalogue for the astrometry and the resulting positional errors are less than 0.1".

We then cross-matched the coordinates-corrected source lists with each other to construct a light curve for each source. We kept only sources with at least five measurements. Figure 3 presents the histogram of the median magnitude, $\langle F850LP \rangle$, of all the sources after the SNR filtering. Due to the drop-off of detected sources beyond 25.7 mag, our sample is photometrically complete down to this magnitude. Since the images used to derive the source lists have different depth (Table 1), we over-plot in Figure 3 the completeness curves of different images with extreme exposure times. We summed the detections of images with exposure times of ~ 2000 s (Prop. ID: 12062) and ~ 5000 s (Prop. ID: 11563), respectively. For both data sets, the number counts of detections decline at magnitudes fainter than the magnitude completeness limit of this work. Thus, the variable depth of the images did not affect our results. The resulting catalogue consists of 21,647 sources. Figure 4 presents the distribution of the number of data points in the light curve, N_p , as a function of the time baseline, T_{bas} , which is defined as the time difference between the first and the last observation of a source. A large fraction of sources ($\sim 80\%$)

³ <http://spiff.rit.edu/match/match-1.0/>

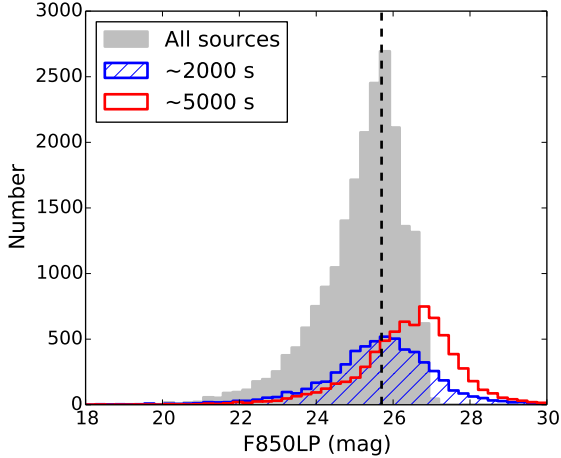


Figure 3. The distribution of the median magnitude, $\langle F850LP \rangle$, of all the sources (gray shaded histogram) along with the completeness curves for images with exposure times of 2000 s (blue hatched) and 5000 s (red), respectively. The dashed line indicates the completeness limit of our final sample.

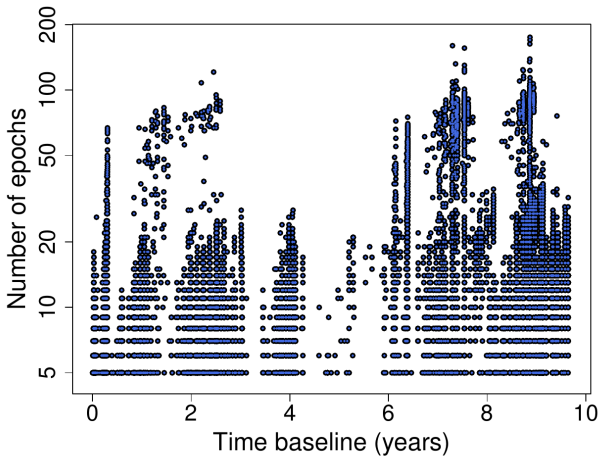


Figure 4. The number of data points as a function of the maximum time baseline covered by the light curve.

has been observed for more than two and up to ten years with a median time baseline of 8.5 years. The average and median number of data points in the light curves are 15 and 12, respectively.

The photometric accuracy was tested by comparing our *MagAper2* magnitudes to those in HSCv2. First, we cross-matched all the sources with HSCv2 using a radius of $1''$, resulting in 7245 matches out of 21,647 final sources (our source list is much deeper than HSCv2 in this region). In Figure 5, we plotted the difference in magnitude, $\langle F850LP \rangle_{\text{this work}} - \langle F850LP \rangle_{\text{HSCv2}}$ as a function of magnitude between this study and HSCv2 and find the values to be comparable. The relation is linear through the full magnitude range as expected. We visually inspected the images and the light curves of the outliers (marked with black filled circles on Figure 5) and attributed the magni-

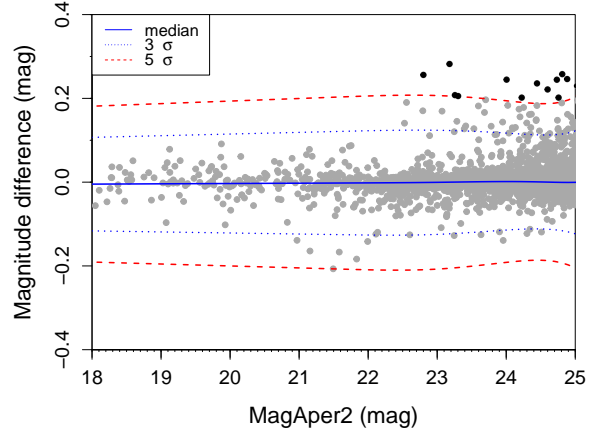


Figure 5. A comparison between the $\langle F850LP \rangle$ magnitude of our photometry and HSCv2. The grey points represent all the sources in common. The blue solid line shows the median, while the blue dotted and red dashed lines represent the 3σ and 5σ values of the magnitude difference, respectively. Sources exceeding the 5σ value are highlighted in black.

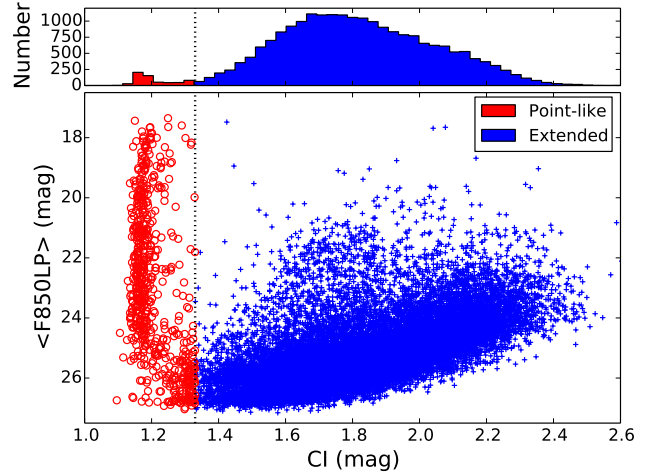


Figure 6. The median magnitude, $\langle F850LP \rangle$, as a function of the *CI* for point-like (red circles) and extended sources (blue crosses). The dashed line represents the chosen threshold at $CI = 1.33$ mag that separates the two populations. The upper panel shows the histogram of the *CI*.

tude discrepancies to multiple detections of the same extended source in the HSCv2.

The separation of the extended and point-like sources was performed using *CI* as defined in the HSC, $CI = \text{MagAper1} - \text{MagAper2}$ (Whitmore et al. 2016). The *CI* histogram reveals two well-defined areas (Figure 6, top panel). We fitted two Gaussians to the two populations (point-like and extended) and the point where these two fits come across is at $CI = 1.33$ mag. Adopting it as the separation threshold results in 21,022 extended and 625 point-like sources. Figure 6 (bottom panel) shows the *CI* as a function of magnitude, where the two populations are plotted using different colours.

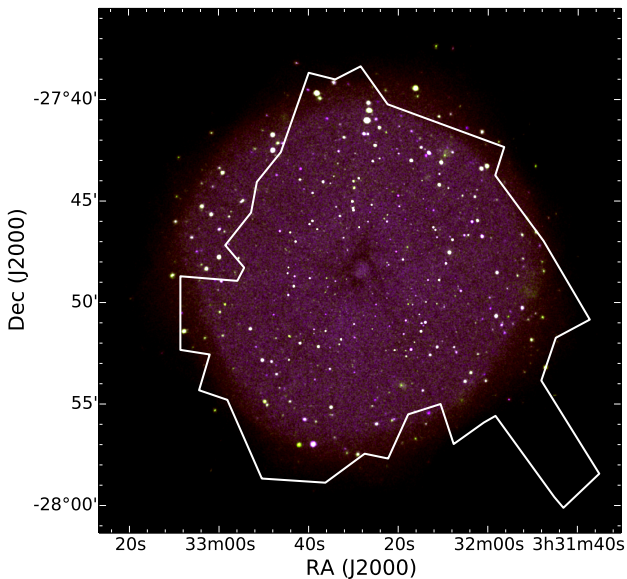


Figure 7. Colour composite image of the exposure corrected and smoothed 7 Ms CDF-S. The white polygon represents the GOODS-S footprint.

2.2 X-ray and IR data sets

GOODS-S is among the deepest and best studied fields in the sky and over the last decades there is a variety of imaging and spectroscopic data available from radio to X-ray wavelengths. In this study, apart from the HST optical observations, we utilize X-ray and IR catalogues and, also, photometric or spectroscopic data when available to validate the nature of the variable sources.

We use four X-ray catalogues from CDF-S and the Extended Chandra Deep field South (ECDF-S) with different depths: 250 ks (Xue et al. 2016), 2 Ms (Luo et al. 2008), 4 Ms (Xue et al. 2011) & 7 Ms (Luo et al. 2017). The area studied in this work partly overlaps with CDF-S, which is centered at $\alpha = 3\text{h}32\text{m}28.06\text{s}$ and $\delta = -27^\circ48'26.4''$ (J2000) and covers an area of ~ 464.5 arcmin². ECDF-S covers an area of 0.54 deg² in the sky centered at $\alpha = 3\text{h}32\text{m}24.0\text{s}$ $\delta = -27^\circ48'47.0''$ (J2000). Figure 7 shows CDF-S and GOODS-S projected on the sky. The catalogues are produced from the X-ray images taken by the Advanced CCD Imaging Spectrometer camera (ACIS, Garmire et al. 2003) aboard the *Chandra X-Ray Observatory*. We also used these four catalogues to test the dependence of the number of optical counterparts on the depth of the X-ray image.

Table 2 presents the number of sources detected in at least one band (the supplementary sources – lower significance X-ray sources with bright IR counterparts – of each catalogue are also included), the number of observations and the observation dates with the on-axis sensitivity limits in the soft (0.5–2 keV), hard (2–8 keV) and broad (0.5–8 keV) bands of the catalogues. The 250 ks catalogue is from ECDF-S, which covers a much larger region, but here we only present the sources that lie within CDF-S. The 7 Ms CDF-S catalogue extends up to 7 keV to avoid the background noise present at higher energies. The full list of the observations of each catalogue and the detailed description of the data reduction can be found in the aforementioned

papers and the references therein. All published catalogues include additional information on the sources, such as X-ray properties, multi-wavelength counterparts and redshifts.

For the variable optical sources identified in Sec. 3 that have no X-ray counterparts, we independently reduced the *Chandra* images using the CIAO software v2.0.1⁴ to construct the 7 Ms image and calculated the X-ray flux upper-limits. First, we created the 7 Ms co-added images in the three bands – broad, soft and hard, starting with the level 2 event files. We used 99 observations taken from October 1999 to March 2016. We kept only the central CCD chips (ccd_id=0,1,2,3) and filtered out flares affecting the background in the light curve of each observation by masking the sources and using the `deflare` tool with the `clean_lc` option. For each observation, we ran the `wavedetect` tool to create source catalogues, so we could reproject the images at the same reference point in the sky to achieve a good absolute astrometric solution. The final step was to combine the event files with the `dmmerge` tool and create images and exposure maps for all the bands.

The smoothed image including all three bands is shown in Figure 7. For the non-detected sources in the X-rays, we measured the counts and the exposure effective areas in a circular region centered on the position of the optical counterparts. The radius, r_i , used for each optical source was calculated in a way that to enclose a specified fraction of the point spread function. The fraction adopted here decreases from the on-axis (0.95) to off-axis sources (0.5). The background was extracted from 500 circular regions (with aperture half of r_i) at random positions around the optical source (within a distance from 1.5 to 5 times of r_i) that do not overlap with other X-ray or the optical variable sources. We derived the count rate for each background region and finally normalized the mean value of all of them to the area of the source. Then we derived the upper limits with a confidence interval of 99.7%. The count rates were converted to fluxes, using an energy conversion factor equal to 2.8×10^{-9} , 1.5×10^{-9} and 6.2×10^{-9} ergs photon⁻¹ for the broad, soft and hard band, respectively by assuming a power-law model with photon index of $\Gamma = 1.7$.

GOODS-S overlaps, also, with the Spitzer IRAC/MUSYC Public Legacy Survey in the Extended Chandra Deep Field South (PI: Pieter van Dokkum, SIMPLE). SIMPLE covers an area of $\sim 1,600$ arcmin² surrounding GOODS-S and contains photometry for $\sim 45,000$ sources from deep Spitzer/IRAC (Fazio et al. 2004) observations combined with other UV to mid-IR data from the Multiwavelength Survey by Yale-Chile (MUSYC). In this work, we use the four IRAC bands (3.6 μm , 4.5 μm , 5.8 μm and 8.0 μm) to construct the IR selected AGN sample (Section 4.2), while the r, J, K and 3.6 μm bands from the same catalogue were used to separate the stellar from the extra-galactic objects in Section 3.2. The full description of these data can be found in Damen et al. (2011).

Table 2. Summary of the basic information of the CDF-S X-ray catalogues.

X-ray catalogue	Number of observations	Observation dates	# sources CDF-S	$F_{0.5-8 \text{ keV}}$ (ergs $\text{cm}^{-2} \text{s}^{-1}$)	$F_{0.5-2 \text{ keV}}$ (ergs $\text{cm}^{-2} \text{s}^{-1}$)	$F_{2-8 \text{ keV}}$ (ergs $\text{cm}^{-2} \text{s}^{-1}$)	# matches optical	# matches variable
250 ks ECDF-S	9	2004	430	$> 3.5 \times 10^{-16}$	$> 1.1 \times 10^{-16}$	$> 6.7 \times 10^{-16}$	144	14
2 Ms CDF-S	23	1999 - 2000	578	$> 7.1 \times 10^{-17}$	$> 1.9 \times 10^{-17}$	$> 1.3 \times 10^{-16}$	298	16
4 Ms CDF-S	54	1999 - 2010	776	$> 3.2 \times 10^{-17}$	$> 9.1 \times 10^{-18}$	$> 5.5 \times 10^{-17}$	464	21
7 Ms CDF-S	102	1999 - 2016	1055	$> 1.9 \times 10^{-17}$	$> 6.4 \times 10^{-18}$	$> 2.7 \times 10^{-17}$	621	24

Note. – The flux limits of the 7 Ms CDF-S catalogue in the broad and the hard band are derived up to 7 keV.

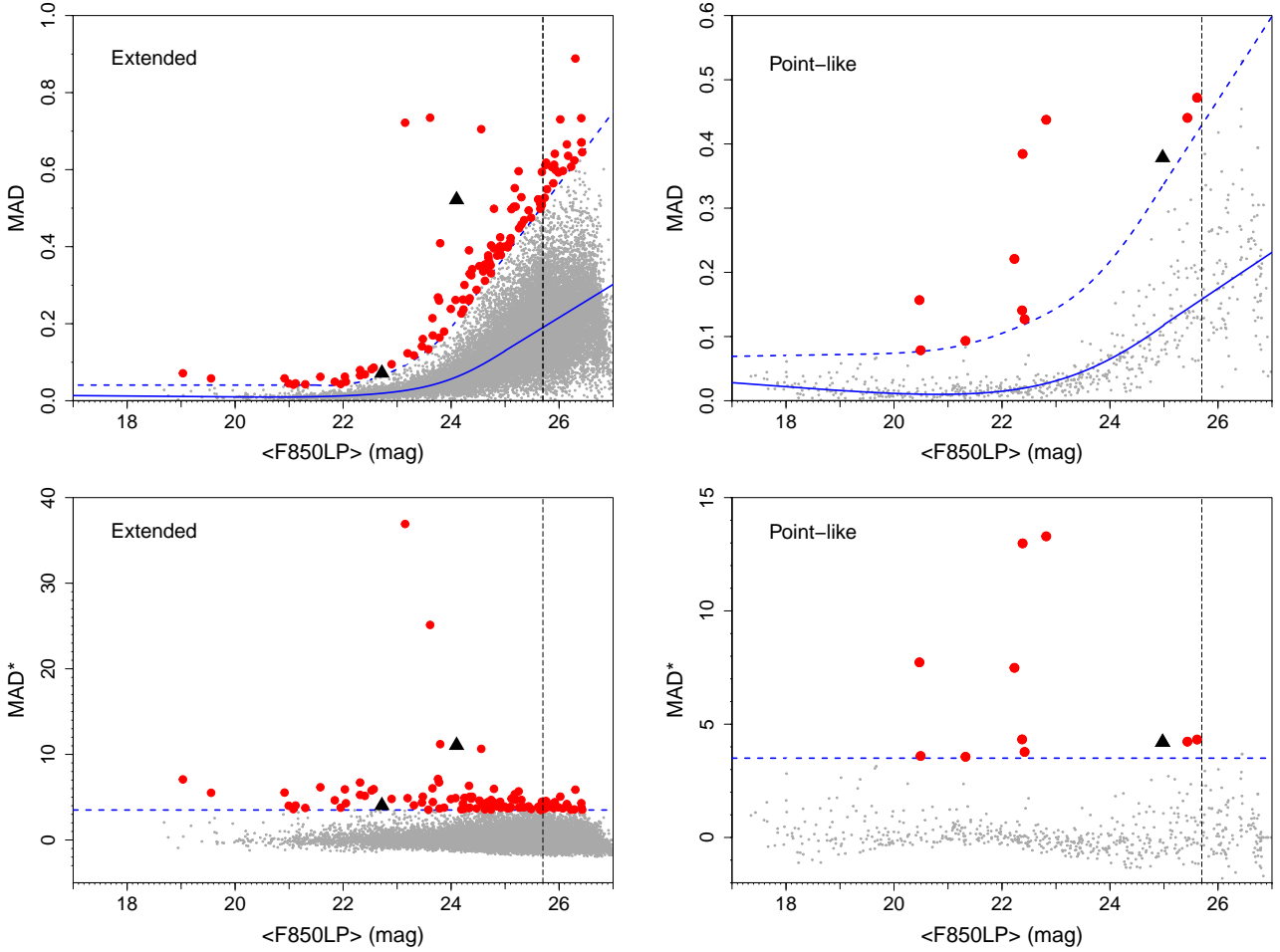


Figure 8. The MAD (upper panels) and normalized significance MAD^* (lower panels) as a function of the median magnitude ($\langle F850LP \rangle$) for the extended (left) and point-like sources (right). All the sources in our survey are shown with grey points, while the AGN candidates are shown with red circles, and the confirmed SNe with black triangles. The blue solid and dashed lines represent the median and the threshold, while the vertical black dashed line the completeness limit of our sample.

3 AGN SELECTION BASED ON OPTICAL VARIABILITY

3.1 Variability method

Sokolovsky et al. (2017b) discussed two classes of statistical methods that quantify variability of a source. The first class quantifies the scatter of the magnitudes within a light curve, while the methods of the second class quantify the smoothness of a light curve by taking into account the order and

time at which the magnitude measurements were obtained. Regular variability can be detected that way too, if the observing cadence is shorter than the variability timescale (Ferreira Lopes & Cross 2016), or, if the scatter is higher than what is expected from noise (Ferreira Lopes & Cross 2017).

Light curve simulations by Sokolovsky et al. (2017b) suggest that the scatter-based methods are more suitable for detection of variability in light curves having a small number of points compared to the methods that character-

⁴ <http://cxc.harvard.edu/ciao>

ize the light curve smoothness. Median Absolute Deviation⁵ (Rousseeuw & Croux 1993, MAD) belongs to the first class of methods. It is the most robust to outliers among the variability indices discussed by Sokolovsky et al. (2017b). In Appendix A1, we compare the performance of various variability-detection statistics in the presence of photometric outliers and find that MAD is a reliable method, resistant to individual outlier measurements.

MAD is defined as the median value of the absolute deviations of the measurements, m_j , from the median:

$$\text{MAD} = b \times \text{median}(|m_j - \text{median}(m_j)|), \quad (1)$$

where $b = 1/(\sqrt{2} \text{erf}^{-1}(1/2)) \approx 1.4826$ is the factor scaling the median absolute deviation to the standard deviation (assuming the normal distribution of m_j); erf^{-1} is the inverse error function.

Specifically, our variability detection algorithm works as follows: we divided the sources into magnitude bins and by assuming a Gaussian distribution, we calculated for each bin the median magnitude, the median MAD and the standard deviation (σ) of MAD. The bin size is adjusted so as to have at least 50 sources in each bin. To get a smooth magnitude dependence, we fitted a cubic spline to the median and the threshold values. We, also, extrapolated toward fainter magnitudes to account for the completeness limit (Section 2). Taking into account that the majority of the sources are normal galaxies and no variations are expected, the variable sources are those that exceed a cut-off above the median. We note that Sarajedini et al. (2011) rely on the same critical assumptions as we do here: that the majority of sources are non-variable and that sources of similar brightness have similar photometric errors. Villforth et al. (2010) also rely on this assumption indirectly when they derive the scaling factors for the estimated photometric errors that they use to compute the C-statistic.

Following Bershady et al. (1998), or more recently Sarajedini et al. (2011), we determine the threshold separately for the point-like and the extended sources (except we determine the threshold in MAD scaled to σ rather than in σ as Sarajedini et al. 2011). Figure 8 (upper panels) shows the variability index, MAD, as a function of the median magnitude, $\langle \text{F850LP} \rangle$ for the extended (left) and point-like (right) sources. We also calculated the normalized significance, MAD^* , for each source through the following formula:

$$\text{MAD}_i^* = \frac{\text{MAD}_i - \text{median}(\text{MAD})_b}{\sigma(\text{MAD})_b}, \quad (2)$$

where MAD_i is the MAD for the i^{th} source and b the corresponding magnitude bin. The significance has units of σ . The plots of MAD^* as a function of magnitude are shown in the lower panels of Figure 8.

We set the threshold of 3.5σ in MAD^* above which we consider the sources to be variable. Assuming the normal distribution of MAD^* we estimate the fraction of sources that are expected to have the value of MAD^* above the

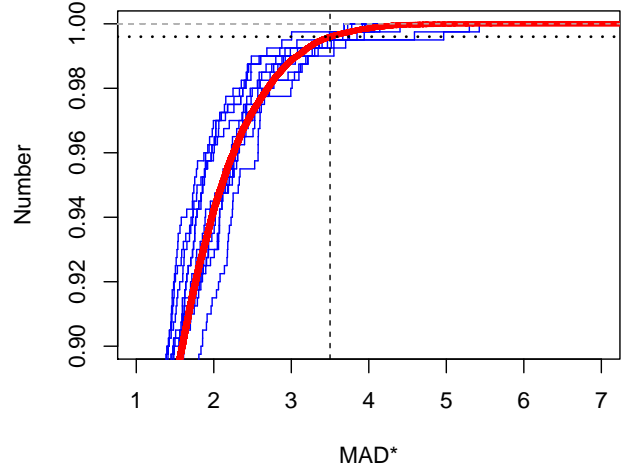


Figure 9. The median cumulative distributions of the normalized significance for under-sampled data with different number of data points in the light-curve (blue thin lines). The red thick line represents the distribution from our final sample, while the horizontal dashed and dotted line represents the statistical significance of 100% and 99.65%, respectively. The vertical line is our 3.5σ threshold.

threshold, i.e. the false positive rate, as:

$$\text{FP}_{\text{rate}} = 1 - \frac{1}{2} \left(1 + \text{erf} \left(\frac{3.5}{\sqrt{2}} \right) \right) \approx 2.3 \times 10^{-4}, \quad (3)$$

so out of 21,022 extended and 625 point-like sources of the initial sample we expect 5 and < 1 false positives among the extended and point-like candidate variable sources, respectively. This corresponds to $\sim 3.2\%$ of the total number of 187 variable candidates. The false positives are expected to have magnitudes near the completeness limit where the majority of sources are found (Fig. 3). Furthermore, as our sample is not homogeneous concerning the number of data points in their light curves, we simulated under-sampled data to check the dependence of the adopted variability threshold on the number of data points (Appendix A2). We found that the thresholds derived from the simulated data were either very close to, or below the adopted variability threshold, indicating the goodness of our threshold.

Moreover, to further explore the genuine statistical significance of our threshold, we calculated the cumulative distributions of the normalized MAD for several magnitude bins with different number of data points ($N=5, 6, 7, 8, 9, 10, 20, 30$ & 40). In Figure 9, we show the median cumulative distributions for different number of data points as long as with the real distribution of our sample. The average statistical significance of the 3.5σ thresholds is 99.65%. However, the true significance should be greater than this value, since the distribution also includes the variable sources. We visually inspected the light curves of all the candidate variable sources and the associated images. We checked for diffraction spikes from nearby foreground stars, close neighbors, poorly removed cosmic rays, proximity to a frame edge and

⁵ https://en.wikipedia.org/wiki/Median_absolute_deviation

saturation or misalignment of individual exposures. All these factors may introduce false variability. Following this procedure, we classified all the variable sources into three categories. Sources with clear variability in their light curve, far from other sources with no artifacts or potential problems recorded and with accumulated significance higher than 99.9%, were assigned grade A (86 sources). Sources with minor problems that may affect the reliability were assigned a grade B (32 sources). This category includes sources that might have centring issues, caused by the extension of the object or that are too faint and dispersed and sources between 3.5 sigma and accumulated significance of 99.9%. Finally, all sources that were found to be affected by saturation, diffraction spikes, blending or other significant problems were assigned a grade C (69 sources).

3.2 Stars and supernovae

In order to separate AGN candidates from stars, we followed Rowan-Robinson et al. (2005) and Damen et al. (2011). According to Rowan-Robinson et al. (2005), stars can be distinguished from the extra-galactic objects, such as QSOs and very distant AGNs by their brightness in the r band ($r < 23$ mag) and their position in the $3.6\mu\text{m}/r$ flux ratio versus the $r-i$ diagram (Figure 10, right). The two populations occupy different regions in the diagram and can be easily separated. This method was also used by Falocco et al. (2015) and Rowan-Robinson et al. (2013). On the other hand, Damen et al. (2011) excluded the stellar population using a colour cut-off ($[J-K](AB) < 0.04\text{mag}$) and applied certain quality criteria to their initial sample: signal-to-noise ratio in K band $(S/N)_K > 5$ and their relative weight in the K band versus the z- band, $wK > 0.5$.

We cross matched our initial catalogue of 21,647 sources with the SIMPLE data (Sec. 2.2) to obtain the colours for our sources and applied the above diagnostics. Figure 10 shows the $[J-K]$ vs. $3.6\mu\text{m}$ and the $3.6\mu\text{m}/r$ vs. $[r-i]$ diagrams with the sources colour coded by the CI. The open black circles presented in the plot are used to show the variable sources in each diagram. Both diagnostics indicated eight classified variable sources to be stars. All of them are grade C variable sources, as six were saturated and two were blended sources. We therefore identify no high-confidence candidate variables among the foreground stars.

For the identification of SNe, we relied on visual inspection of the light curves and the corresponding images. We found three sources with light curves of Grade A resembling SNe (ID 7343, 9581 & 14446), which have all been previously reported in the literature by Strolger et al. (2004) and Riess et al. (2007). Their light curves and observational properties can be found in Figure B1 and Table B1 in the Appendix B. Out of the SNe catalogues, there are 13 more SNe that have a counterpart in our initial sample, but they are all below the variability threshold. Possible explanations could be the differences in the observation dates (the peak was not observed), or that our variability algorithm could not detect variability if the number of the data points in the light curve that correspond to the peak was small and they were considered as outliers by MAD. For these sources, we also calculated the standard deviation, but they were still below the threshold, thus the first case is more likely to happen.

In the next sections, we proceed with the analysis of the remaining 113 variable sources (10 point-like and 103 extended), which are presumed to be AGN candidates (Table 3). Figure 11 illustrates the positions of the variable sources on the sky, while some examples of the AGN light curves can be found in Figure 12.

4 PROPERTIES OF THE AGN CANDIDATES

4.1 X-ray detections & upper limits

We cross-matched the final sample of the 113 AGN candidates with the four X-ray catalogues described in Section 2.2. We used a search radius of $2''$ as the maximal positional error of the X-ray sources reaches values of $\sim 1.8''$ that corresponds to high off-axis angles. The positional errors of our optically variable sources are less than $0.1''$. In order to check if the X-ray counterparts are the correct ones, we visually checked both optical and X-ray images. We excluded two X-ray counterparts that corresponded to neighbouring sources, resulting in a total of 26 AGN candidates with X-ray emission. The counterparts in the 7 Ms catalogue include all the sources from the lower depth catalogues, except for two sources detected in the 250 ks and 4 Ms catalogues. According to Luo et al. (2017), they do not exist in the 7 Ms catalogue, because they are variable sources or they are spurious detections resulting from background fluctuations or they did not pass the binomial no-source probability threshold used. The number of the X-ray counterparts is listed in Table 2 and increases with depth, as expected. All the variable point-like sources, except for two (ID: 2816 and 19102 with optical magnitude greater than 25 mag), have X-ray counterparts and also have been identified as QSOs or AGNs in other studies, including Villforth et al. (2010), Trevese et al. (2008) and Sarajedini et al. (2011). It is worth noting that four optically variable AGN candidates (ID 7270, 11168, 11213 & 19673) have been selected as X-ray variable sources in Young et al. (2012), while two out of those (ID 11168 & 11213) are present also in the variability-selected LLAGN catalogue of Ding et al. (2018).

A well-known diagnostic to identify AGNs is the F_X/F_{opt} diagram (Maccacaro et al. 1988; Barger et al. 2003; Hornschemeier et al. 2003), where F_X and F_{opt} are the X-ray and optical flux, respectively. The conventional AGN population lies in the area between $\log(F_X/F_{\text{opt}}) = \pm 1$, while spectroscopically confirmed AGN have been reported up to $\log(F_X/F_{\text{opt}}) = \pm 2$. The normal galaxies are expected to have $\log(F_X/F_{\text{opt}}) \leq -2$. In Figure 13, we plot the optical flux (F850LP) as a function of the X-ray (0.5-8 keV) flux of our optically variable AGNs compared with the normal galaxy (filled green squares) and AGN (open black squares) populations from Luo et al. (2017). The optically variable AGNs with X-ray detections (filled red circles) lie over the whole area within $F_X/F_{\text{opt}} = \pm 2$. We could be quite confident that sources with $F_X/F_{\text{opt}} > -1$ are AGNs, while between -2 and -1 their flux ratio is still consistent with AGNs, but their nature is confirmed by the combination of variability with X-ray emission.

The flux upper limits (open blue circles) are consistent with AGNs according to their F_X/F_{opt} ratio, though deeper X-ray images are needed to detect them. In particu-

Table 3. Catalogue of the variable AGN candidates.

ID	Grade	RA	Dec	N _p	T _{bas}	CI	<F850LP>	MAD*	z	z Ref.	F _x [0.5-8 keV]
(1)	(2)	(J2000)	(J2000)	(5)	(years)	(mag)	(mag)	(σ)	(10)	(11)	(ergs cm ⁻² s ⁻¹)
		(3)	(4)			(7)	(8)	(9)			(12)
347	B	52.94086	-27.85703	5	9.1	2.22	22.56	5.93	0.58	3,c	<7.40E-16
398	A	52.94348	-27.81377	6	9.12	2.19	23.31	4.04	0.89	3,c	<4.86E-16
561	A	52.95213	-27.84881	8	9.11	1.7	24.55	10.6	0.2	3,g	<4.44E-16
615	A	52.95474	-27.95340	6	1.92	2.14	22.4	5.15	1.22	1,e	2.10E-015
1081	A	52.96888	-27.77844	5	8.18	2.01	22.03	5.91	0.67	1,a	3.17E-015
1181	B	52.97121	-27.85896	5	9.11	2.03	24.32	3.71	1.3	3,c	<2.40E-16
1560	B	52.98128	-27.90919	5	9.13	1.64	25.67	3.64	0.95	3,c	<4.65E-16
1749	A	52.98486	-27.76583	6	1.95	1.57	23.14	36.9	4.83	3,c	<2.72E-16
1799	A	52.98585	-27.88607	6	9.11	2.26	22.31	6.71	0.24	1,c	<1.31E-16
2300	B	52.99559	-27.71783	6	8.3	2.28	23.77	6.72	1.03	3,d	<3.05E-16
2644	A	53.00151	-27.72218	9	2.51	1.28	22.23	7.5	1.04	1,a	1.46E-014
2816	A	53.00463	-27.74807	9	8.46	1.29	25.43	4.23	0.66	3,a	<2.01E-16
3129	A	53.00967	-27.87611	5	9.14	1.47	23.78	3.67	1.43	1,a	1.06E-015
3240	A	53.01125	-27.72273	9	8.58	1.69	25.76	4.54	2.17	3,b	<1.92E-16
3268	A	53.01156	-27.70921	7	8.58	1.64	25.65	3.63	2.9	3,b	<4.20E-16
3485	B	53.01471	-27.86247	5	9.14	2.17	23.65	6.03	1.33	3,d	<3.52E-16
3753	A	53.01887	-27.77287	6	8.46	1.57	26.16	3.88	1.16	3,b	<2.98E-16
4080	A	53.02418	-27.76962	7	1.06	1.56	25.86	4.19	1.3	3,b	<1.44E-16
4210	A	53.02684	-27.87276	5	9.14	2.01	24.59	4.08	2.33	3,c	<3.02E-16
4388	B	53.02974	-27.78371	5	8.03	1.66	25.89	3.71	3.67	3,b	<1.67E-16
4422	A	53.03039	-27.91629	5	8.99	2.16	24.08	4.89	1.14	3,c	<2.66E-16
4757	A	53.03535	-27.79084	5	9.07	1.68	25.92	4.41	3.08	3,d	<1.38E-15
4949	A	53.03939	-27.80194	16	9.58	1.18	20.47	7.73	2.81	1,a	6.51E-015
4981	A	53.03997	-27.81762	5	1.11	1.73	26.3	5.87	0.3	3,b	<1.65E-16
5182	A	53.04340	-27.80370	5	0.9	1.57	26.02	5.06	1.47	3,b	<1.59E-16
5281	A	53.04498	-27.79240	19	9.58	1.99	24.9	3.99	0.81	3,b	<9.88E-17
5322	A	53.04550	-27.73754	11	8.59	1.26	22.42	3.78	1.62	1,a	1.95E-014
5497	A	53.04805	-27.80435	14	9.57	1.86	21.84	4.63	0.54	1,a	3.78E-017
5510	B	53.04824	-27.77309	11	9.44	2.21	23.47	5.06	1.21	2,b	<7.72E-16
5664	A	53.05076	-27.89412	5	9.19	2.08	23.75	7.13	1.1	3,c	<1.82E-16
5856	B	53.05383	-27.75002	22	2.52	2.13	24.34	3.77	1.2	2,b	<2.87E-16
6061	B	53.05739	-27.71684	5	2.5	1.69	25.73	3.64	1.55	3,b	<2.74E-16
6381	A	53.06216	-27.81900	12	9.39	1.79	25.06	3.73	1.05	3,b	<9.72E-17
6446	A	53.06299	-27.77906	34	9.33	2.06	24.39	5.04	0.96	2,b	<5.29E-17
6515	A	53.06407	-27.71645	12	8.59	1.82	24.62	4.27	2.55	3,d	<1.45E-16
6932	B	53.07015	-27.73988	5	2.44	1.62	25.48	3.6	0.76	3,b	<2.17E-16
7112	B	53.07239	-27.71873	14	8.59	2.33	22.89	4.79	0.64	1,b	<6.74E-15
7224	A	53.07367	-27.70253	10	8.59	2.05	23.66	4.43	1.18	1,d	<2.06E-16
7270	A	53.07447	-27.84984	17	9.51	2.39	20.91	5.53	0.12	1,a	1.58E-016
7531	B	53.07825	-27.87013	14	9.64	2.17	23.99	4.77	0.66	1,d	<2.67E-16
7588	A	53.07909	-27.75488	12	9.33	1.86	25.43	3.92	1.18	3,b	<1.89E-16
7906	B	53.08332	-27.94113	5	3.82	1.85	23.19	4.88	0.65	3,b	<1.46E-16
7924	A	53.08366	-27.86983	6	9.51	1.78	25.16	4.77	0.73	1,c	<1.24E-16
7938	A	53.08386	-27.73963	20	2.51	2.26	23.86	3.77	1.21	1,a	1.46E-016
7947	B	53.08388	-27.78481	5	9.08	1.44	25.77	3.79	2.3	3,b	<1.47E-16
8184	A	53.08716	-27.78490	18	9.33	2.14	22.31	5.26	0.66	1,a	4.15E-017
8240	A	53.08781	-27.89646	7	3.98	1.58	25.98	3.8	4.33	3,b	<1.32E-16
8413	A	53.09017	-27.84784	20	9.64	2.19	24.18	3.56	1.03	3,c	3.75E-017
8728	A	53.09443	-27.67175	8	2.6	1.9	24.9	4.46	1.35	3,c	<3.54E-16
8850	A	53.09608	-27.88041	15	9.11	1.51	25.1	3.86	0.02	3,d	<3.08E-16
8917	A	53.09674	-27.77237	26	9.33	1.93	24.73	3.51	0.6	2,b	<1.76E-16
9014	B	53.09825	-27.77718	5	2.21	2.14	24.22	3.63	0.42	1,f	<1.74E-16
9021	A	53.09840	-27.86258	7	9.08	1.62	25.68	4.47	1.12	3,b	<1.17E-16
9239	A	53.10137	-27.85917	6	9.08	1.56	25.74	4.51	0.9	3,b	<1.45E-16
9288	B	53.10213	-27.72846	5	2.26	1.74	25.25	3.79	1.08	1,f	<1.96E-16
9630	B	53.10628	-27.86994	5	2.25	1.92	25.11	4.82	1.33	3,d	<2.41E-16
9757	A	53.10780	-27.83883	32	9.64	2.25	23.57	3.54	1.09	1,a	3.75E-017
9764	A	53.10784	-27.72622	15	8.59	1.8	24.47	3.69	1.21	1,a	9.52E-017
10122	B	53.11194	-27.76271	8	8.86	1.98	25.17	5.34	1.3	1,d	<1.49E-16
10144	A	53.11215	-27.71111	12	8.59	2.27	23.79	11.2	1.6	2,b	<3.22E-16
10240	A	53.11330	-27.89131	26	9.11	1.89	24.62	3.56	2.19	2,b	<1.28E-16
10426	A	53.11540	-27.88511	5	3.72	1.52	25.9	4.16	1.29	3,b	<1.88E-16
10463	A	53.11578	-27.70676	11	8.59	1.43	25.19	4.67	0.12	3,d	<1.78E-16

Note. – (1): Identifier. (2): Quality grade. (3): Right ascension. (4): Declination. (5): Number of data points in the light curve. (6): Time baseline. (7): Concentration index. (8): Median magnitude in the F850LP filter. (9): Normalized MAD. (10): Redshift. (11): Method used to compute z (1: spectroscopy, 2: grism and 3: photometry), while the letter refers to the paper where the redshift obtained (a: Luo et al. (2017), b: Momcheva et al. (2016), c: Cardamone et al. (2011), d: Straatman et al. (2017), e: Xue et al. (2016), f: Taylor et al. (2009) and g: Wolf et al. (2008)). (12): Flux in the X-ray [0.5-8 keV] band. The '<' symbol represent the flux upper limit.

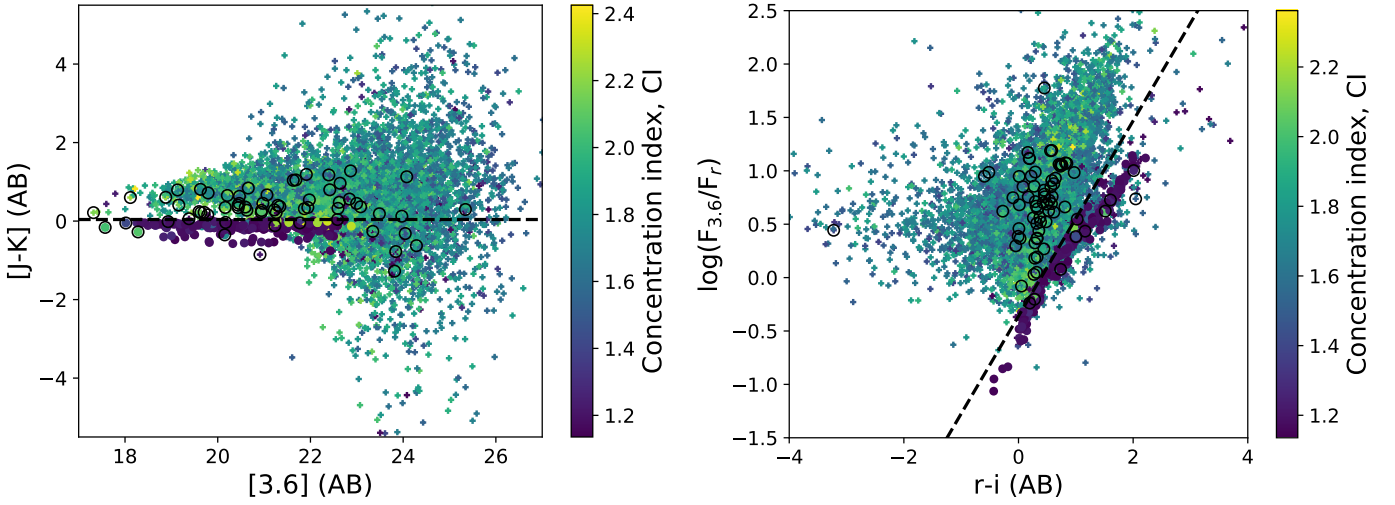


Figure 10. The $[J - K]$ versus $3.6\mu\text{m}$ diagram (left) and the $3.6\mu\text{m}/r$ flux ratio versus $r - i$ diagram (right). The crosses represent the common sources between our sample and the SIMPLE data. The filled circles are the sources classified as stars. All sources are colour coded by the CI. The open black circles indicate the variable sources.

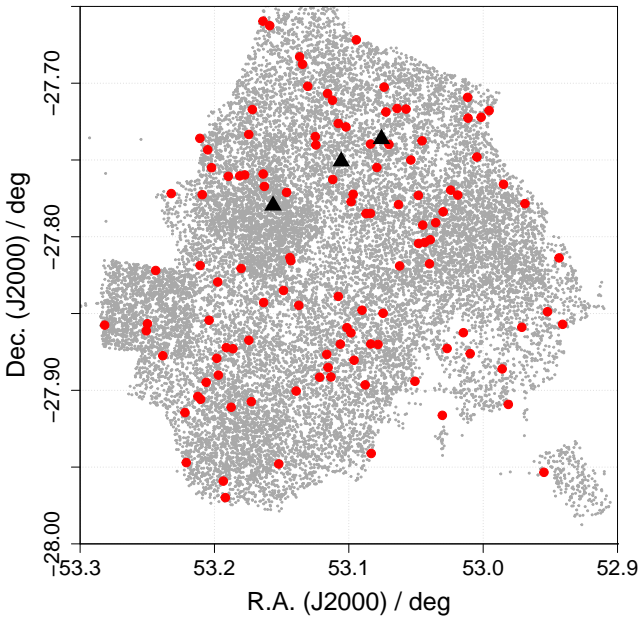


Figure 11. Spatial distribution of the AGN candidates (red circles). The confirmed SNe are shown with black triangles. The background grey points represent the whole sample consisting of 21,647 sources.

lar, the majority of the flux upper limits lie below the average $F_X/F_{\text{opt}} = 0$ line, indicating that these AGNs are mostly X-ray weak. Concerning the sources that overlap with the normal galaxies, Luo et al. (2017) mentioned that a fraction of the normal galaxy population may also include LLAGNs. For the sources detected only in the soft or hard band, we transformed the fluxes into the $[0.5-8 \text{ keV}]$ band using

the WebPIMMS⁶ v4.8d software, assuming the photon index $\Gamma = 1.4$ and the Galactic HI column density $n_H = 10^{20} \text{ cm}^{-2}$. The same transformations were applied to the broad band (0.5 – 7 keV) of Luo et al. (2017).

To further understand the nature of these sources, we cross-matched our AGN candidates with the catalogue of Momcheva et al. (2016) to associate each source with the corresponding redshift of the host galaxy. Their catalogue provides the best redshift among grism, ground-based spectroscopic or photometric redshifts (Skelton et al. 2014). For the candidates with X-ray counterparts, we used the spectroscopic redshifts provided by Luo et al. (2017). The redshifts of some sources that did not have a match in the previous catalogues, were recovered from Straatman et al. (2017), Cardamone et al. (2011), Taylor et al. (2009) and Wolf et al. (2008). We found published redshifts for all the variability-selected AGN candidates: 63 sources have photometric redshifts, while for the remaining 60 sources the redshifts were derived from spectra.

Even though the available spectra from Momcheva et al. (2016) and the other catalogues are capable to provide secure redshifts, the width of the lines is too noisy for the classification of our optically faint AGN sample (broad or narrow lines). The redshift distribution for the AGN candidates is presented in Figure 14 with the distribution of all the X-ray sample of the 7Ms CDF-S catalogue that have an optical counterpart in GOODS-S for comparison. The AGNs with not yet detected X-ray emission extend to higher redshifts.

Figure 15 shows the magnitude distribution of the candidate AGNs and also the magnitude distribution of the X-ray sample reported in Luo et al. (2017) with an optical counterpart in GOODS-S (both AGNs and normal galaxies). It is very clear that the sample with X-ray upper limits is optically fainter than the AGN candidates with X-ray detec-

⁶ <https://heasarc.gsfc.nasa.gov/docs/software/tools/pimms.html>

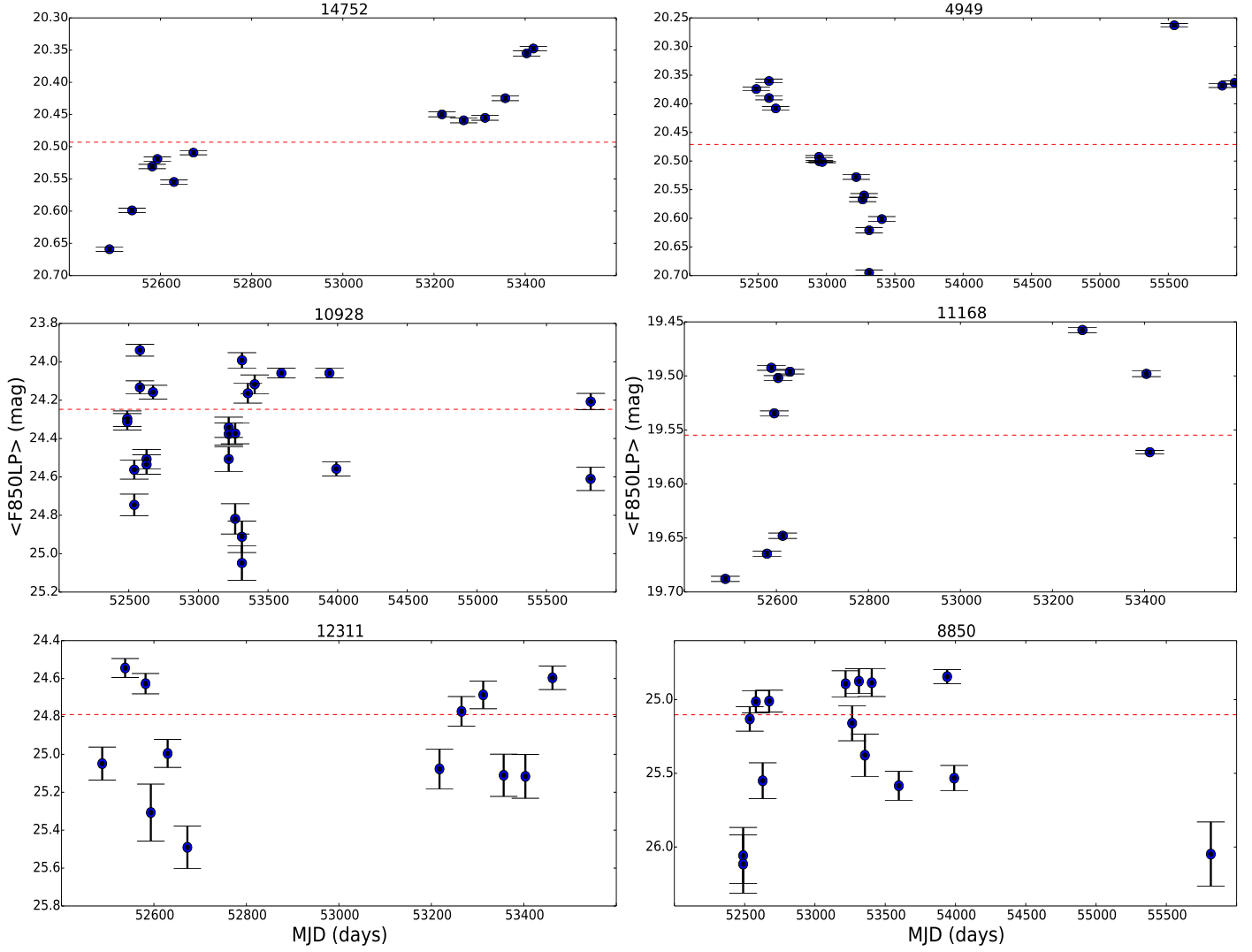


Figure 12. Example light curves of the AGN candidates. The dashed line indicates the median magnitude and the number on the top of each plot indicates the identifier of the source.

tions. The redshift and magnitude distributions suggest that the optical surveys, such as HST, may be able to identify faint high-redshift AGNs through variability. These AGNs would have been missed by current X-ray studies. Since faint nuclear emission can be observed in the optical, there are no obscuration at all or very weak obscuration effect by dust, thus these AGNs are likely LLAGNs. Their position in the F_X/F_{opt} diagram suggests that these high-redshifted intrinsically X-ray weak AGNs lie below the conventional AGN population (around $F_X/F_{\text{opt}} = 0$), and thus, the dependence on redshift and X-ray flux should be considered when working with F_X/F_{opt} diagrams.

We next estimated the X-ray luminosity [2-10 keV] of all the AGN candidates. We found the sample of variable sources with X-ray detections and upper limits to be distributed over ~ 5.5 and ~ 4.5 orders of luminosity, from $10^{39.5}$ to 10^{45} ergs s^{-1} and $10^{38.5}$ to 10^{43} ergs s^{-1} , respectively, with mean values of 1.77×10^{42} and 4.57×10^{41} ergs s^{-1} . In Figure 16, we compare our luminosity distribution with the distribution of different populations of AGNs located in

the nearby universe ($z \sim 0$): Seyfert galaxies (Panessa et al. 2006) and LLAGNs (González-Martín et al. 2015) that include type I and II of LINERs and Seyferts. The luminosities of the AGN candidates detected here on the basis of optical variability lie within the range of the latter sub-classes of AGNs, denoting further evidence of AGN activity even at these low X-ray luminosities.

4.2 Mid-infrared selected AGN

In addition to studying their X-ray properties, we explore whether our optically variable AGN candidates show evidence of accretion onto a supermassive black hole via their infrared emission. The mid-IR emission from AGNs, in particular after the advent of sensitive spectrographs in space telescopes such as *ISO* and *Spitzer*, has proven extremely useful in revealing the presence of an AGN and characterising whether it is of type I or type II (Clavel et al. 2000; Verma et al. 2005; Weedman et al. 2005; Wu et al. 2009; Alonso-Herrero et al. 2016). It is now widely accepted that

Table 3 – continued

ID	Grade	RA (J2000)	Dec (J2000)	N_p	T_{bas} (years)	CI (mag)	<F850LP> (mag)	MAD* (σ)	z	z Ref.	F_x [0.5-8 keV] (ergs cm ⁻² s ⁻¹)
(1)	(2)	(3)	(4)	(5)	(6)	(7)	(8)	(9)	(10)	(11)	(12)
10511	A	53.11638	-27.87660	14	9.32	2.21	22.52	5.78	0.38	1,a	<8.85E-17
10928	B	53.12174	-27.89144	24	9.11	2.23	24.24	4.92	1.03	3,d	<2.70E-16
11168	A	53.12448	-27.74021	10	2.52	2.31	19.55	5.51	0.07	1,a	6.95E-016
11213	A	53.12494	-27.73476	5	2.27	2.35	19.03	7.07	0.07	1,a	5.12E-016
12113	A	53.13448	-27.68765	11	2.66	2.1	24.69	4.32	0.96	2,b	3.61E-016
12311	B	53.13659	-27.68284	12	2.66	1.9	24.78	4.39	0.67	3,d	<4.09E-16
12361	A	53.13720	-27.84469	22	9.33	2.04	23.46	4.36	2.03	1,a	8.05E-017
12540	A	53.13916	-27.90047	26	9.12	1.93	24.34	5.03	1.33	2,b	<5.83E-17
12911	A	53.14316	-27.81556	28	8.73	1.91	24.85	3.91	4.14	1,b	<1.35E-16
12977	A	53.14385	-27.81352	52	8.73	2.28	21.11	4.02	0.2	3,b	<2.06E-16
13240	B	53.14633	-27.77111	8	2.29	2.21	24.73	3.88	1.31	1,d	<1.32E-16
13505	A	53.14860	-27.83498	7	8.47	1.96	25.09	3.74	0.06	3,b	<1.67E-16
13941	B	53.15214	-27.94796	12	3.91	2.24	21.29	3.74	0.12	1,c	<2.92E-16
14752	A	53.15884	-27.66252	12	2.55	1.18	20.49	3.59	0.84	1,a	4.63E-014
15280	A	53.16286	-27.76722	82	8.87	1.23	21.32	3.3	1.22	1,a	7.93E-015
15342	A	53.16340	-27.84283	13	8.85	1.57	24.98	3.89	0.13	3,b	<2.63E-16
15390	B	53.16373	-27.75912	94	8.86	1.98	24.37	4.82	1.03	3,d	<2.51E-16
15405	A	53.16386	-27.65959	8	2.54	1.71	25.25	5.68	1.1	3,b	<1.44E-15
16363	B	53.17179	-27.71713	5	2.28	1.75	25.3	4.68	1.28	3,b	<2.54E-16
16466	A	53.17258	-27.90738	11	2.5	1.51	26.41	4.3	0.08	3,b	<2.99E-16
16705	A	53.17438	-27.86740	13	9.12	1.23	22.37	4.33	3.61	1,a	5.74E-015
16721	A	53.17445	-27.73336	22	8.85	1.34	24.9	4.13	2.57	1,a	2.68E-015
17058	A	53.17742	-27.75976	10	7.29	1.62	26.14	4.19	2.51	3,b	<1.42E-16
17370	A	53.18014	-27.82066	15	8.86	1.3	22.82	13.33	1.92	1,a	9.28E-015
17472	B	53.18116	-27.76034	5	6.9	1.71	26.28	3.57	2.62	3,b	<1.20E-16
17999	A	53.18626	-27.87292	28	4.06	1.92	24.52	4.6	2.05	1,b	<1.17E-16
18125	A	53.18755	-27.91102	23	9.12	2.39	21.07	3.6	0.45	1,a	2.07E-016
18467	A	53.19124	-27.87216	14	9.12	2	24.21	4.23	0.98	2,b	<3.50E-16
18541	A	53.19188	-27.96988	6	2.73	1.61	24.79	5.96	0.21	3,c	<6.89E-16
18687	B	53.19341	-27.95913	6	0.85	1.96	22.05	4.29	0.65	3,c	<5.09E-16
19006	B	53.19706	-27.89010	16	9.12	1.99	24.67	3.92	1.29	2,b	<2.42E-16
19047	A	53.19754	-27.82945	6	2.69	1.55	25.67	3.55	0.24	3,b	<1.16E-16
19102	A	53.19828	-27.87916	12	9.13	1.25	25.61	4.32	1.04	3,b	<3.02E-16
19429	B	53.20216	-27.75500	5	8.6	1.9	25.3	3.8	2.19	3,d	<1.78E-16
19579	A	53.20396	-27.85437	21	9.12	2.16	24.33	6.32	1.37	2,b	<1.76E-16
19673	A	53.20503	-27.74339	12	8.57	2.24	21.95	3.76	0.21	1,a	1.71E-016
19762	B	53.20616	-27.89478	5	0.61	1.68	25.93	3.97	1.45	3,b	<5.02E-16
19976	A	53.20908	-27.77260	7	7.29	1.48	26.42	3.51	5	3,b	<1.43E-16
20057	A	53.21029	-27.90583	15	3.98	2.28	20.99	4	0.12	1,b	<3.90E-16
20076	A	53.21064	-27.81873	7	8.35	1.52	26.22	3.52	2.84	3,b	<4.87E-17
20085	A	53.21084	-27.73590	6	8.57	1.72	24.92	3.75	1.08	3,b	<2.36E-16
20190	A	53.21235	-27.90401	24	3.98	2.04	24.68	4.45	1.68	2,b	<3.47E-16
20698	A	53.22099	-27.94706	6	0.85	1.51	23.61	25.1	0.35	3,c	<4.47E-16
20760	B	53.22195	-27.91449	5	2.5	1.77	25.65	3.5	0.85	3,d	<2.57E-15
21288	A	53.23217	-27.77188	6	8.71	1.75	24.74	4.67	0.58	3,c	<2.16E-16
21541	A	53.23844	-27.87746	10	9.08	2.07	24.7	4.09	0.77	2,b	<3.49E-16
21733	A	53.24374	-27.82197	14	1.04	1.53	26.07	3.69	0.95	3,g	<2.07E-16
21944	B	53.24986	-27.85666	24	8.98	2.03	25.04	3.68	1.25	3,d	<2.74E-16
21983	B	53.25070	-27.86125	27	8.98	2.27	21.57	6.16	0.01	2,b	<5.51E-16
22884	A	53.28173	-27.85756	9	8.81	1.24	22.38	13.02	1.61	1,a	2.07E-014

Note. – (1): Identifier. (2): Quality grade. (3): Right ascension. (4): Declination. (5): Number of data points in the light curve. (6): Time baseline. (7): Concentration index. (8): Median magnitude in the F850LP filter. (9): Normalized MAD. (10): Redshift. (11): Method used to compute z (1: spectroscopy, 2: grism and 3: photometry), while the letter refers to the paper where the redshift obtained (a: Luo et al. (2017), b: Momcheva et al. (2016), c: Cardamone et al. (2011), d: Straatman et al. (2017), e: Xue et al. (2016), f: Taylor et al. (2009) and g: Wolf et al. (2008)). (12): Flux in the X-ray [0.5-8 keV] band. The '<' symbol represent the flux upper limit.

the AGN continuum emission appears as a power law from the 3 to 10 μm range, since the strong UV and X-ray radiation destroys the molecules responsible for the Polycyclic Aromatic Hydrocarbon (PAH) emission, while heating the surrounding dust particles in thermal equilibrium to near dust sublimation temperatures. The mid-IR AGN spectrum may also display absorption features with variable strength (due to astronomical silicates at 9.7 and 18 μm) depending on the geometry of the obscuring dust as well as the lumi-

nosity of the active nucleus compared with the host galaxy (Nenkova et al. 2008a,b).

Even when mid-IR spectra are not available, one may use mid-IR broad-band colours to trace this slope. A number of such diagnostics have been proposed using the IRAC instrument (Fazio et al. 2004) on board the *Spitzer* Space Telescope (Werner et al. 2004) which provided imaging at 3.6, 4.5, 5.8 and 8.0 μm for a large sample of galaxies. These include the "Lacy wedge" (Lacy et al. 2004, 2007; Sajina et al. 2005), the "Stern wedge" (Stern et al. 2005) and more

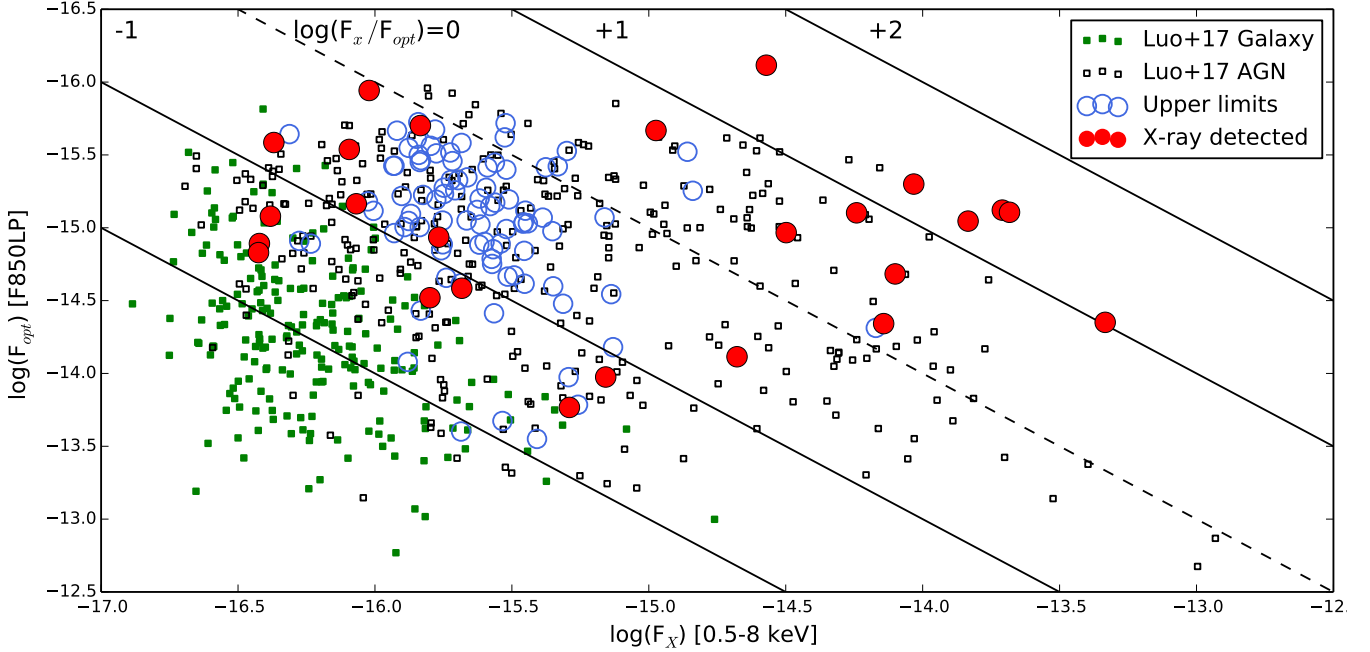


Figure 13. Broad (0.5-8 keV) X-ray vs. optical ($\langle F850LP \rangle$) flux for the 26 AGN candidates with X-ray counterparts (red circles). Open blue circles represent those sources for which only upper limits were derived. The open black and filled green squares in the background represent the sources classified as AGN or normal galaxies in Luo et al. (2017), respectively. The dashed line indicates the $\log(F_X/F_{opt}) = 0$ and the solid lines from left to right correspond to $\log(F_X/F_{opt}) = -2, -1, +1, +2$, respectively. The fluxes are given in units of $\text{ergs cm}^{-2} \text{s}^{-1}$.

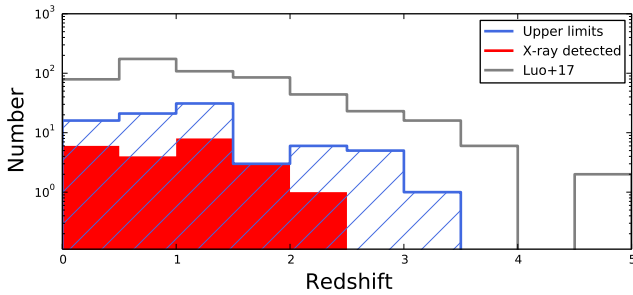


Figure 14. Redshift distribution for the candidate AGNs with (filled red) and without (hatch-filled blue) X-ray counterparts. The grey histogram indicates all the X-ray sources with optical counterparts in GOODS-S.

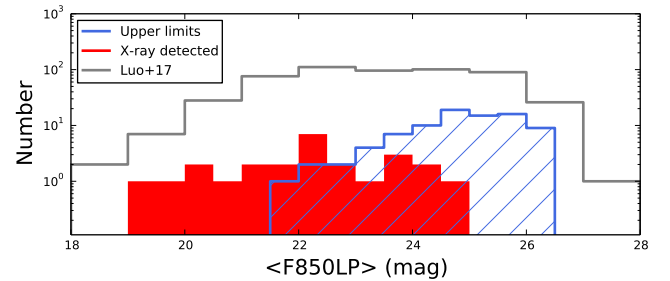


Figure 15. Median F850LP magnitude distribution for the candidate AGNs with (red filled) and without (blue hatch-filled) X-ray counterparts. The grey histogram indicates all the X-ray sources with optical counterparts in GOODS-S.

recently the "Donley wedge" (Donley et al. 2007, 2012). Similar methods have also been proposed for sources observed with WISE (Stern et al. 2012; Assef et al. 2013; Mateos et al. 2012). We examine our candidates using the diagnostic of Donley et al. (2012), which has proven to be the most robust for a rather wide redshift range. The criteria by Lacy et al. (2007) are also used, for comparison.

We used the SIMPLE data mentioned in Section 2.2. This sample is photometrically complete at $5 \mu\text{Jy}$, where there is a turn-over in the number density plot of the fluxes in the [5.8] band. Furthermore, we restricted our analysis to 3,904 mid-IR sources (IR sample) that have detections at all four IRAC channels as well as an optical HST counterpart with five or more data points in the light curve identified

by our survey. Out of the IR sample, there are 41 optically variable sources. Following the AGN selection criteria by Donley et al. (2012):

1. $x > 0.08$ and $y > 0.15$
2. $y > (1.21 * x) - 0.27$ and $y < (1.21 * x) + 0.27$
3. $f[4.5] > f[3.6]$ and $f[5.8] > f[4.5]$ and $f[8.0] > f[5.8]$,

where $x = \log(f[5.8]/f[3.6])$, $y = \log(f[8.0]/f[4.5])$ and $f[\text{band}]$ is the flux of the corresponding band, we found 53 sources (hereafter, Donley IR AGNs). Out of those, 37 have X-ray counterparts, while five sources are optical variables. The latter five sources have also been detected in X-rays (in the 7Ms image) and are classified as QSOs in the literature. The optical variability can be explained by their QSO nature;

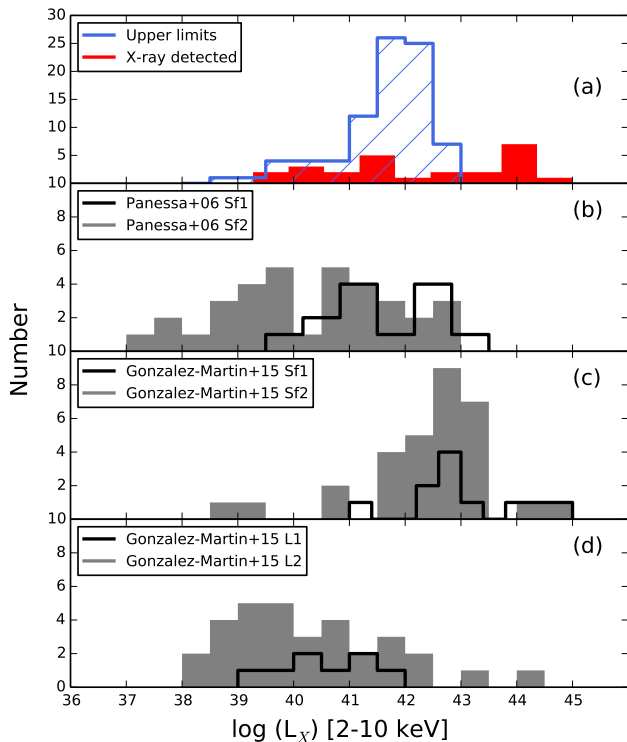


Figure 16. X-ray luminosities in the [2-10 keV] band (panel a) for the AGN candidates, with (red filled) and 3σ upper limits (blue hatch-filled) X-ray counterparts. In panel (b) the luminosity distributions of Seyfert galaxies are shown from Panessa et al. (2006). Panel (c) and (d) represent the galaxy population of Seyferts and LINERs derived from González-Martín et al. (2015). The black and shaded grey histograms indicate the type I and II, respectively.

i.e. direct view to the central source. At the same time the powerful AGN heats the dusty torus (seen face on) and its reprocessed emission dominates the infrared emission from the host galaxy.

Lacy et al. (2007) used a similar mid-IR colour-colour diagram with somewhat relaxed limits and without the power law condition:

1. $x > -0.1$ and $y > -0.2$
2. $y > (0.8 * x) - 0.5$.

Among the 770 sources that fulfill these criteria (hereafter, Lacy IR AGNs), there are 188 X-ray detections and 13 optically variable AGNs according to our analysis. The Lacy IR AGNs contains all 53 Donley IR AGNs. Figure 17 shows the IRAC 4-band colour-colour plot for the IR sample. The lines represent the wedges as defined in Lacy et al. (2007) and Donley et al. (2012). We also over-plotted the optically variable, Donley IR and the X-ray selected AGNs.

5 DISCUSSION

5.1 Comparison with previous variability studies

We compared our variable sources with other variability studies of GOODS-S, including Villforth et al. (2010) and

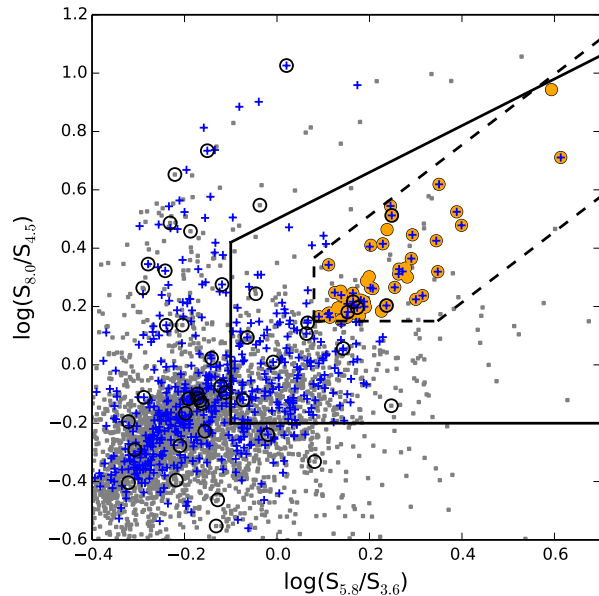


Figure 17. IRAC colour-colour diagram of the IR sample (gray points). The Lacy IR AGNs defined by the solid line. The Donley IR AGNs are those inside the dashed line and follow an IR power-law (filled orange circles). The optically variable and the X-ray selected AGN samples are represented by open circles and blue crosses, respectively.

Sarajedini et al. (2011), who also searched for optical variability in this field. Out of the 88 variable sources reported by Villforth et al. (2010), 86 sources were included in our initial sample of 21,647 sources. Out of these, $\sim 8\%$ were identified as variable with our method. Similarly, out of the 42 variable sources of Sarajedini et al. (2011) in common with our initial sample, we recovered $\sim 17\%$. In a larger field of view, Trevese et al. (2008) found 132 variable sources, 23 of which lie in the area studied in this work and are included in our survey; we find eight sources to be variable in our catalogue. Regarding the sample of Falocco et al. (2015), there is only one common source with our survey, which is classified as non-variable by our variability detection algorithm.

The main differences between our study and the studies of Villforth et al. (2010) and Sarajedini et al. (2011) lie in the source detection algorithm and the larger amount of data. Our approach to identifying variable objects among a set of light curves is similar to the one used by Sarajedini et al. (2011) with two important modifications: 1) we used MAD as the measure of the light-curve scatter to filter out individual outliers and 2) we used the median instead of mean to determine the expected value of scatter in a given magnitude bin. Villforth et al. (2010) used C statistics that rely mostly on the estimated photometric uncertainties to select variables, while Sarajedini et al. (2011) used the classic standard deviation on V-band imaging data. Both used a 3σ vs. a more secure threshold of 3.5σ employed in this work. In order to check the dependence of the recovery rate and the false-positive contamination by the adopted variability threshold, we calculated the recovery rate of both studies and also the percentage of the false positive rate out of the

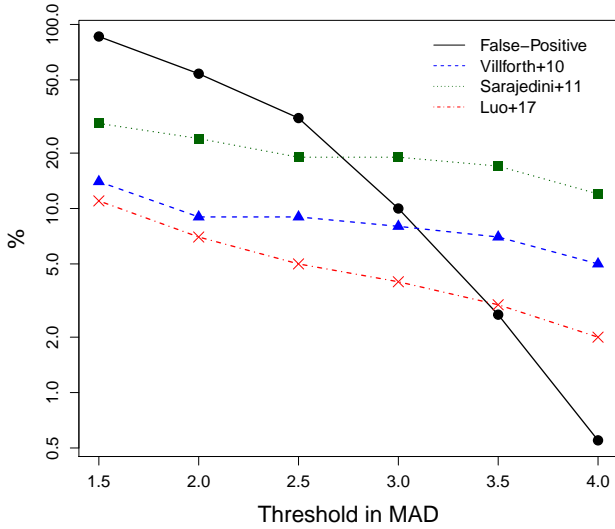


Figure 18. Percentage of false positive rate (black circles), recovery rate of variable sources identified by Villforth et al. (2010) (blue triangles) and Sarajedini et al. (2011) (green squares) and percentage of X-ray sources by Luo et al. (2017) (red crosses) identified as variables in this study as a function of different values of thresholds. The y-axis is in logarithmic scale.

variable sources (as described in Section 3.1) for different values of the threshold. In Figure 18, we plot the results. By relaxing the threshold to lower values ($\text{MAD} \approx 2.5$), the recovery rate remains almost the same for both studies (1-2% difference), though the false positive rate rapidly increases. The threshold of 3.5 that we have adopted ensured that the false-positive contamination was kept below 5%.

The larger amount of data are due to the larger area included in this work, which doubled the number of sources, and the longer time baseline of the light curves. In particular, we used observations spanning up to ten years, instead of six months, increasing the number of points in the light curves, so we expect to detect new sources with higher sensitivity at longer timescales. Furthermore, the data reduction – source detection and photometry – differs from that employed in the previous studies. We used SExtractor, since it is better suited for detecting extended sources compared to IRAF. Moreover, we used images from the latest HLA data release, which is the first one to take into account the misalignments between both single exposures and filters⁷. Thus, the quality of the images used in this work and, consequently, the reliability of our photometry are supposed to be much higher than previous studies.

5.2 X-ray, mid-IR and optical variability selected AGNs

To facilitate a direct comparison and present the various selection methods in a uniform manner, we selected the Donley IR, Lacy IR and X-ray detected AGNs that lie inside the

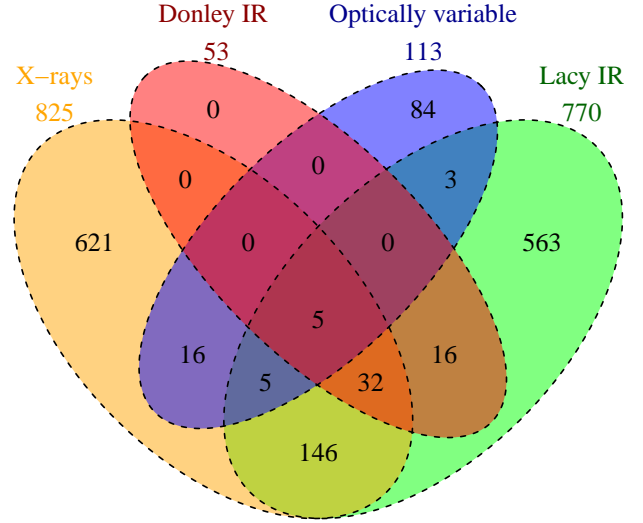


Figure 19. Venn diagram of the AGN samples selected through optical variability (blue), X-rays (orange), Donley et al. (2012) (red) and Lacy et al. (2007) (green) IR criteria.

area of GOODS-S along with the optical variable AGN candidates. In Figure 19, we demonstrate the overlapping of the optical variability (113), Donley IR (53), Lacy IR (770) and X-ray selected (825) AGN samples with a Venn diagram.

The deepest available X-ray catalogue contains 825 sources in the area of GOODS-S. 621 sources have optical counterparts with five or more data points in their light curve, while 587 have both optical and IR detections. We found $\sim 3.5\%$ of the X-ray sources having significant optical variability (Figure 18 shows also this percentage as a function of the variability threshold). On the other hand, among the 113 optical variable AGN candidates, 26 have X-ray counterparts ($\sim 23\%$). Optical variability could identify AGNs through a wide range of magnitudes and, especially, the AGN population that is missed by X-rays ($\sim 75\%$). This result comes from current X-ray survey depths. To visually demonstrate this dependence, in Figure 20 we show the fraction of variable sources that are X-ray detected in the four catalogues with various depths, divided into different magnitude bins. For the magnitude bins in the bright end, the fraction reaches values of about $\sim 70\%$, while at fainter magnitude bins there are no X-ray detections. Villforth et al. (2012) and Trevese et al. (2008) found similar results, while Sarajedini et al. (2011) had a higher rate of variable sources with X-ray detections. Out of the variable sample of Falocco et al. (2015), less than 10% had X-ray counterparts, and in the COSMOS field, De Cicco et al. (2015) reached a high percentage, up to $\sim 75\%$. However, their sample had a magnitude limit in the r band at $r \leq 23$ mag. Given the same limits in the magnitude, we derive almost the same completeness with respect to X-rays (Figure 20).

Furthermore, in this work we set a $3.5\text{-}\sigma$ cut-off in MAD to identify variables. Given a less conservative value of the cut-off, the percentage of X-ray detected sources in the variable sample increases. In particular, a $3\text{-}\sigma$ cut-off increases the X-ray detected sources to 30%. However, at the same time the false positive variability rate also increases signifi-

⁷ http://hla.stsci.edu/hla_faq.html

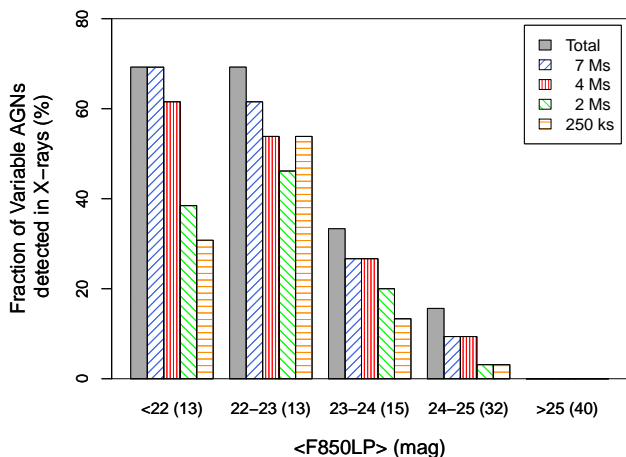


Figure 20. The fraction of AGNs selected through optical variability divided into five magnitude bins that are X-ray detected in catalogues of different depths. The number of optically variable AGNs in each bin are shown in the parentheses.

cantly. To avoid a high incidence of false variables, we necessarily miss a population of X-ray detected AGNs which display lower optical variability. Future surveys with higher sensitivities and better sampled data with longer time baselines will allow us to identify individually variable objects and fully characterize their variability properties without taking into account the whole population statistics. In that case, variability will be able to recover the X-ray detected AGN population with low significance (either low redshifted or high luminous AGNs).

Regarding the IR selected AGNs, the Lacy et al. (2007) method selected a large number of AGN candidates through colour-colour criteria (770), comparable to that of X-ray AGNs. 25% of these are X-ray detected, while the majority of the X-ray sources fall outside the Lacy wedge (Fig. 17). Despite the large number of AGN candidates, the contamination of star-forming galaxies is expected to be as high as 80% (Donley et al. 2012), as the sensitivity limit of our IR sample is at $5 \mu Jy$. Donley et al. (2012) studied the star-forming contamination of the IR selected AGNs defined by Lacy et al. (2007) and Stern et al. (2005) for samples with different depths and revised these criteria by adding an additional power law criterion. Thus, the Donley IR sample of 53 sources is expected to only have $\sim 10\%$ contamination as stated by Donley et al. (2012). Out of those, 37 have X-ray emission ($\sim 70\%$) and all of them are included in the Lacy IR sample. It is noteworthy to say that the Donley wedge contains sources that are selected by the Lacy et al. (2007) criteria, but fail the power law criterion of Donley et al. (2012). One third of the variable sample had detections at all four IRAC bands (41/113). The percentage of the variable sources common between the Donley and Lacy IR AGNs is $\sim 12\%$ and $\sim 32\%$, respectively, while the majority of the variable sources fall outside both wedges (Figure 17) compared to previous ground-based variability studies (Falocco et al. 2016). This implies that the optical variability based on HST observations is capable to identify AGNs deep into the IR region where other selection methods fail.

It is obvious that different methods are at some level sensitive to different types of objects (different luminosities,

different redshifts, different dust content along the line of sight, etc.). X-ray selection is by far the most robust technique resulting in a high number of AGNs. However, there is a large fraction of optically variables and IR selected AGNs that are not detected in X-rays. These sources are likely highly obscured or low-luminosity AGNs. The Lacy et al. (2007) diagnostic also returns a large sample of AGN candidates, but the contamination from star-forming galaxies is very high considering the depth of this study. At shallower depths, the contamination is minimized (Donley et al. 2012). On the other hand, the AGN sample selected by Donley et al. (2012) is highly complete and reliable having no contamination. However, it picks only a small sample of luminous, unobscured and obscured AGNs and misses the LLAGNs. Finally, optical variability returns a large sample of AGNs less obscured, moderate luminosity and redshift and is capable of identifying LLAGNs, which are missed by the other methods due to the currently survey depths.

6 SUMMARY AND CONCLUSIONS

Variability is a basic property of AGNs and has been proven to be a reliable method to reveal non-obscured LLAGNs. Many studies assembled multi-epoch data and used variability to identify AGNs. The need, though, for highest photometric accuracy and long-term observational monitoring impose limits on the completeness of such surveys. Previously in the GOODS South field, Villforth et al. (2010, 2012) and Sarajedini et al. (2003, 2011) used a five epoch dataset (*i*- and *z*-band, respectively) spanning six months. In a larger area and from ground-based telescopes, Falocco et al. (2015) used, also, a six month baseline, while Trevese et al. (2008) used a longer time baseline of two years.

In this work, we substantially increased the time baseline by up to ten years using deep HST observations (*z*-band). We created a new catalogue of optically variable AGN candidates in the GOODS-S. We used SExtractor to construct the light curves of $\sim 22,000$ sources. The Median Absolute Deviation was utilized to search for variability as it has the highest performance among the other variability indices in the presence of outliers. A 3.5σ cut-off was applied to identify variable sources. Our results can be summarized as follows:

- We identified 116 high confidence variable sources. After removing three known Supernovae, we ended up with 113 AGN candidates (103 extended and ten point-like).
- We explored the mid-IR properties of our AGN candidates. 41 sources have been detected in all four *Spitzer*/IRAC bands and, out of those, 13 and five sources are classified as AGNs through the colour selection adopted by Lacy et al. (2007) and Donley et al. (2012), respectively. Also, the space observations compared to ground-based studies identify AGNs deep into the IR region when other methods fail.
- We cross-matched our AGN sample with the published X-ray catalogues (CDF-S 2, 4 & 7 Ms and ECDFS 250 ks) and found 26 variable sources with X-ray counterparts. This corresponds to $\sim 23\%$ (26/113).
- For all the sources without X-ray detections, we used the 7 Ms image in CDF-S and estimated the flux upper limits using a confidence level of 99.7%. These sources are optically fainter with higher redshifts up to $z=4$.

- The X-ray to optical flux ratios revealed that the variable sources are consistent with the AGN population, as they lie within the area of $-2 < \log(F_X/F_{\text{opt}}) < +2$, but their average $\log(F_X/F_{\text{opt}})$ ratio suggests that high-redshifted intrinsically X-ray weak AGNs lie below the conventional $\log(F_X/F_{\text{opt}}) = 0$ area.
- The X-ray luminosities of our variable AGN candidates are comparable to those of LLAGNs in the Local Universe (Panessa et al. 2006; González-Martín et al. 2015). Hence, the variability in deep optical photometric data is a promising method of finding optically low luminosity AGNs, which the X-ray observations may miss.

We conclude that the different methods (optical variability, IR, X-rays) used to identify AGNs are complementary to each other and equally important to constrain the full picture of the AGN demographics. In particular, optical variability is able to identify a large number of LLAGNs at high redshifts. These are critical for studying the faint end of the AGN luminosity function and it might be the key between normal galaxies and AGNs.

This work is part of the European Space Agency (ESA) project “*Hubble* Catalogue of Variables” (HCV, Sokolovsky et al. 2017a; Gavras et al. 2017), which aims to identify variable sources (stars, transients, Supernovae, AGN, etc.) from the Hubble Source Catalogue (HSC, Whitmore et al. 2016), through different filters and instruments. The HCV targeted fields are more than 250 and the number of sources included exceeds 3.5 million. Specifically for AGNs, there are more than 30 bona-fide deep fields covered by multi-wavelength data with observing time baselines more than two years. Extrapolating our results to these fields, we expect to identify more than 2,000 new AGNs with a high fraction of them being LLAGNs. The variability detection technique used in this work may be applied not only to HST observations but also to other surveys such as the Large Synoptic Survey Telescope (Ivezić et al. 2008, LSST).

ACKNOWLEDGMENTS

The authors are grateful to the anonymous referee for valuable suggestions that significantly improved the manuscript. E. Pouliaxis acknowledges financial support by ESA under the HCV programme, contract no. 4000112940. This research has made use of the VizieR catalogue access tool, CDS, Strasbourg, France. The original description of the VizieR service is presented by Ochenbein et al. (2000). This research has made use of the SIMBAD database (Wenger et al. 2000), operated at CDS, Strasbourg, France and, also, of NASA’s Astrophysics Data System. This research made use of Astropy, a community-developed core Python package for Astronomy (Astropy Collaboration et al. 2013, <http://www.astropy.org>). This publication made use of TOPCAT (Taylor 2005) for all table manipulation. This work is based (in part) on observations made with the Spitzer Space Telescope, which is operated by the Jet Propulsion Laboratory, California Institute of Technology under a contract with NASA. The plots in this publication were produced using Matplotlib, a Python library for publication quality

graphics (Hunter 2007) and R⁸. This work was supported in part by Michigan State University through computational resources provided by the Institute for Cyber-Enabled Research.

REFERENCES

- Alexander T., 1995, *MNRAS*, 274, 909
 Alexander D. M., 2017, *Astronomische Nachrichten*, 338, 172
 Alonso-Herrero A., et al., 2006, *ApJ*, 640, 167
 Alonso-Herrero A., et al., 2016, *MNRAS*, 455, 563
 Assef R. J., et al., 2013, *ApJ*, 772, 26
 Baldassare V. F., Geha M., Greene J., 2018, preprint, ([arXiv:1808.09578](https://arxiv.org/abs/1808.09578))
 Barger A. J., et al., 2003, *AJ*, 126, 632
 Barth A. J., Ho L. C., Rutledge R. E., Sargent W. L. W., 2004, *ApJ*, 607, 90
 Bauer A., Baltay C., Coppi P., Ellman N., Jerke J., Rabinowitz D., Scalzo R., 2009, *ApJ*, 696, 1241
 Bershadsky M. A., Trevese D., Kron R. G., 1998, *ApJ*, 496, 103
 Bertin E., Arnouts S., 1996, *A&AS*, 117, 393
 Bertin E., Arnouts S., 2010, SExtractor: Source Extractor, Astrophysics Source Code Library (ascl:1010.064)
 Brandt W. N., Alexander D. M., 2015, *A&ARv*, 23, 1
 Cardamone C. N., et al., 2011, VizieR Online Data Catalog, 218
 Chatterjee R., Roychowdhury A., Chandra S., Sinha A., 2018, *ApJ*, 859, L21
 Clavel J., et al., 2000, *A&A*, 357, 839
 Cristiani S., Vio R., Andreani P., 1990, *AJ*, 100, 56
 Cristiani S., Trentini S., La Franca F., Andreani P., 1997, *A&A*, 321, 123
 Damen M., et al., 2011, *ApJ*, 727, 1
 De Cicco D., et al., 2015, *A&A*, 574, A112
 Ding N., et al., 2018, *ApJ*, 868, 88
 Dong X., et al., 2007, *ApJ*, 657, 700
 Donley J. L., Rieke G. H., Pérez-González P. G., Rigby J. R., Alonso-Herrero A., 2007, *ApJ*, 660, 167
 Donley J. L., et al., 2012, *ApJ*, 748, 142
 Dressler A., 1989, in Osterbrock D. E., Miller J. S., eds, IAU Symposium Vol. 134, Active Galactic Nuclei. p. 217
 Falocco S., et al., 2015, *A&A*, 579, A115
 Falocco S., et al., 2016, *The Universe of Digital Sky Surveys*, 42, 275
 Fazio G. G., et al., 2004, *ApJS*, 154, 10
 Ferrarese L., Ford H., 2005, *Space Sci. Rev.*, 116, 523
 Ferrarese L., Merritt D., 2000, *ApJ*, 539, L9
 Ferreira Lopes C. E., Cross N. J. G., 2016, *A&A*, 586, A36
 Ferreira Lopes C. E., Cross N. J. G., 2017, *A&A*, 604, A121
 Filippenko A. V., Ho L. C., 2003, *ApJ*, 588, L13
 Finke J. D., Becker P. A., 2014, *ApJ*, 791, 21
 Ford H. C., et al., 1998, in Bely P. Y., Breckinridge J. B., eds, Proc. SPIE Vol. 3356, Space Telescopes and Instruments V. pp 234–248, doi:10.1117/12.324464
 Fruchter A. S., Hook R. N., 2002, *PASP*, 114, 144
 García-González J., Alonso-Herrero A., Pérez-González P. G., Hernán-Caballero A., Sarajedini V. L., Villar V., 2014, in Highlights of Spanish Astrophysics VIII, Proc. of the XI Scientific Meeting of the Spanish Astronomical Society,
 Garmire G. P., Bautz M. W., Ford P. G., Nousek J. A., Ricker Jr. G. R., 2003, in Truemper J. E., Tananbaum H. D., eds, Proc. SPIE Vol. 4851, X-Ray and Gamma-Ray Telescopes and Instruments for Astronomy. pp 28–44, doi:10.1117/12.461599

⁸ R Core Team (2016). R: A language and environment for statistical computing. R Foundation for Statistical Computing, Vienna, Austria. URL <https://www.R-project.org/>.

- Gavras P., et al., 2017, in IAU Symposium. pp 369–372 ([arXiv:1703.00258](#)), [doi:10.1017/S1743921316012746](#)
- Gebhardt K., et al., 2000, *ApJ*, **539**, L13
- Giavalisco M., et al., 2004, *ApJ*, **600**, L93
- Giveon U., Maoz D., Kaspi S., Netzer H., Smith P. S., 1999, *MNRAS*, **306**, 637
- González-Martín O., et al., 2015, *A&A*, **578**, A74
- Graham A. W., Driver S. P., 2007, *ApJ*, **655**, 77
- Graham M. J., Djorgovski S. G., Drake A. J., Mahabal A. A., Chang M., Stern D., Donalek C., Glikman E., 2014, *MNRAS*, **439**, 703
- Greene J. E., Ho L. C., 2004, *ApJ*, **610**, 722
- Greene J. E., Ho L. C., 2007, *ApJ*, **670**, 92
- Greene J. E., Ho L. C., Barth A. J., 2008, *ApJ*, **688**, 159
- Gu M. F., Li S.-L., 2013, *A&A*, **554**, A51
- Gültekin K., et al., 2009, *ApJ*, **698**, 198
- Häring N., Rix H.-W., 2004, *ApJ*, **604**, L89
- Hawkins M. R. S., 1993, *Nature*, **366**, 242
- Helfand D. J., Stone R. P. S., Willman B., White R. L., Becker R. H., Price T., Gregg M. D., McMahon R. G., 2001, *AJ*, **121**, 1872
- Hook I. M., McMahon R. G., Boyle B. J., Irwin M. J., 1994, *MNRAS*, **268**, 305
- Hornschemeier A. E., et al., 2003, *AJ*, **126**, 575
- Hunter J. D., 2007, *Computing In Science & Engineering*, **9**, 90
- Ivezić Ž., et al., 2008, preprint, ([arXiv:0805.2366](#))
- Kasliwal V., Vogeley M., T. Richards G., 2015, *Monthly Notices of the Royal Astronomical Society*, 451
- Kawaguchi T., Mineshige S., Umemura M., Turner E. L., 1998, *ApJ*, **504**, 671
- Kelly B. C., Bechtold J., Siemiginowska A., 2009, *ApJ*, **698**, 895
- Kelly B. C., Becker A. C., Sobolewska M., Siemiginowska A., Uttley P., 2014, *ApJ*, **788**, 33
- Kim J., Karouzos M., Im M., Choi C., Kim D., Jun H. D., Lee J. H., Mezcuca M., 2018, preprint, ([arXiv:1809.01350](#))
- Komossa S., 2015, *Journal of High Energy Astrophysics*, **7**, 148
- Kormendy J., Ho L. C., 2013, *ARA&A*, **51**, 511
- Kormendy J., Kennicutt Jr. R. C., 2004, *ARA&A*, **42**, 603
- Kormendy J., Richstone D., 1995, *ARA&A*, **33**, 581
- Kozłowski S., 2016, *Monthly Notices of the Royal Astronomical Society*, 459, stw819
- Lacy M., et al., 2004, *ApJS*, **154**, 166
- Lacy M., Petric A. O., Sajina A., Canalizo G., Storrie-Lombardi L. J., Armus L., Fadda D., Marleau F. R., 2007, *AJ*, **133**, 186
- Lasker B. M., et al., 2008, *AJ*, **136**, 735
- Lawrence A., Papadakis I., 1993, *ApJ*, **414**, L85
- Li S.-L., Cao X., 2008, *MNRAS*, **387**, L41
- Luo B., et al., 2008, *ApJS*, **179**, 19
- Luo B., et al., 2017, *ApJS*, **228**, 2
- MacLeod C. L., et al., 2010, *The Astrophysical Journal*, **721**, 1014
- MacLeod C. L., et al., 2012, *ApJ*, **753**, 106
- Maccacaro T., Gioia I. M., Wolter A., Zamorani G., Stocke J. T., 1988, *ApJ*, **326**, 680
- Magorrian J., et al., 1998, *AJ*, **115**, 2285
- Marconi A., Hunt L. K., 2003, *ApJ*, **589**, L21
- Mateos S., et al., 2012, *MNRAS*, **426**, 3271
- Middei R., Vagnetti F., Bianchi S., La Franca F., Paolillo M., Ursini F., 2017, *A&A*, **599**, A82
- Momcheva I. G., et al., 2016, *ApJS*, **225**, 27
- Nenkova M., Sirocky M. M., Ivezić Ž., Elitzur M., 2008a, *ApJ*, **685**, 147
- Nenkova M., Sirocky M. M., Nikutta R., Ivezić Ž., Elitzur M., 2008b, *ApJ*, **685**, 160
- Ochsenbein F., Bauer P., Marcout J., 2000, *A&AS*, **143**, 23
- Panessa F., Bassani L., Cappi M., Dadina M., Barcons X., Carrera F. J., Ho L. C., Iwasawa K., 2006, *A&A*, **455**, 173
- Paolillo M., Schreier E. J., Giacconi R., Koekemoer A. M., Grogin N. A., 2004, *ApJ*, **611**, 93
- Paolillo M., et al., 2017, *MNRAS*, **471**, 4398
- Park J., Tripp S., 2017, *ApJ*, **834**, 157
- Rees M. J., 1984, *ARA&A*, **22**, 471
- Richards G. T., et al., 2002, *AJ*, **123**, 2945
- Richards G. T., et al., 2005, *MNRAS*, **360**, 839
- Riess A. G., et al., 2007, *ApJ*, **659**, 98
- Rousseeuw P. J., Croux C., 1993, *Journal of the American Statistical Association*, **88**, 1273
- Rowan-Robinson M., et al., 2005, *AJ*, **129**, 1183
- Rowan-Robinson M., Gonzalez-Solares E., Vaccari M., Marchetti L., 2013, *Monthly Notices of the Royal Astronomical Society*, **428**, 1958
- Sajina A., Lacy M., Scott D., 2005, *ApJ*, **621**, 256
- Sarajedini V. L., Gilliland R. L., Kasm C., 2003, *ApJ*, **599**, 173
- Sarajedini V. L., Koo D. C., Klesman A. J., Laird E. S., Perez Gonzalez P. G., Mozena M., 2011, *ApJ*, **731**, 97
- Schneider D. P., et al., 2007, *AJ*, **134**, 102
- Schneider D. P., et al., 2010, *AJ*, **139**, 2360
- Simm T., et al., 2015, *A&A*, **584**, A106
- Simm T., Salvato M., Saglia R., Ponti G., Lanzuisi G., Trakhtenbrot B., Nandra K., Bender R., 2016, *A&A*, **585**, A129
- Skelton R. E., et al., 2014, *ApJS*, **214**, 24
- Sokolovsky K., et al., 2017a, in European Physical Journal Web of Conferences. p. 02005 ([arXiv:1703.02038](#)), [doi:10.1051/epjconf/201715202005](#)
- Sokolovsky K. V., et al., 2017b, *MNRAS*, **464**, 274
- Stern D., et al., 2005, *ApJ*, **631**, 163
- Stern D., et al., 2012, *ApJ*, **753**, 30
- Straatman C. M. S., et al., 2017, *VizieR Online Data Catalog*, **183**
- Strolger L.-G., et al., 2004, *ApJ*, **613**, 200
- Taylor M. B., 2005, in Shopbell P., Britton M., Ebert R., eds, *Astronomical Society of the Pacific Conference Series Vol. 347, Astronomical Data Analysis Software and Systems XIV*. p. 29
- Taylor E. N., et al., 2009, *ApJS*, **183**, 295
- Terlevich R., Tenorio-Tagle G., Franco J., Melnick J., 1992, *MNRAS*, **255**, 713
- Tremaine S., et al., 2002, *ApJ*, **574**, 740
- Trevese D., Kron R. G., Majewski S. R., Bershadsky M. A., Koo D. C., 1994, *ApJ*, **433**, 494
- Trevese D., Boutsia K., Vagnetti F., Cappellaro E., Puccetti S., 2008, *A&A*, **488**, 73
- Ulrich M.-H., Maraschi L., Urry C. M., 1997, *ARA&A*, **35**, 445
- Vagnetti F., Middei R., Antonucci M., Paolillo M., Serafinelli R., 2016, *A&A*, **593**, A55
- Valdes F. G., Campusano L. E., Velasquez J. D., Stetson P. B., 1995, *PASP*, **107**, 1119
- Vanden Berk D. E., et al., 2004, *ApJ*, **601**, 692
- Verma A., Charmandaris V., Klaas U., Lutz D., Haas M., 2005, *Space Sci. Rev.*, **119**, 355
- Villforth C., Koekemoer A. M., Grogin N. A., 2010, *ApJ*, **723**, 737
- Villforth C., Sarajedini V., Koekemoer A., 2012, *MNRAS*, **426**, 360
- Weedman D. W., et al., 2005, *ApJ*, **633**, 706
- Wenger M., et al., 2000, *A&AS*, **143**, 9
- Werner M. W., et al., 2004, *ApJS*, **154**, 1
- Whitmore B. C., et al., 2016, *AJ*, **151**, 134
- Wolf C., Hildebrandt H., Taylor E. N., Meisenheimer K., 2008, *A&A*, **492**, 933
- Wu Y., Charmandaris V., Huang J., Spinoglio L., Tommasin S., 2009, *ApJ*, **701**, 658
- Xue Y. Q., et al., 2011, *ApJS*, **195**, 10
- Xue Y. Q., Luo B., Brandt W. N., Alexander D. M., Bauer F. E., Lehmer B. D., Yang G., 2016, *ApJS*, **224**, 15
- Young M., et al., 2012, *ApJ*, **748**, 124
- Zuo W., Wu X.-B., Liu Y.-Q., Jiao C.-L., 2012, *ApJ*, **758**, 104
- de Diego J. A., 2010, *AJ*, **139**, 1269

de Vries W. H., Becker R. H., White R. L., Loomis C., 2005, *AJ*, 129, 615

di Clemente A., Giallongo E., Natali G., Trevese D., Vagnetti F., 1996, *ApJ*, 463, 466

van Dokkum P. G., 2001, *PASP*, 113, 1420

APPENDIX A: VARIABILITY DETECTION SIMULATIONS

A1 Variability detection in the presence of outlier measurements

For all but the faintest optical sources, the accuracy of their brightness measurements is limited by the poorly constrained systematic effects rather than the number of collected photons (“shot noise”) and uncertainties in the background level estimations. This means we typically do not have a reliable error bar attached to a photometric measurement. Of a particular concern in the context of HST photometry are the residual cosmic rays that were not cleaned-out perfectly in the process of image stacking (“drizzling”; Fruchter & Hook 2002) that overlap with the measured image of the object. To circumvent the above issues, we may 1) assume that in a non-crowded field like GOODS-S (Sec. 1) objects of similar brightness will have similar measurement errors and the majority of objects are non-variable; 2) employ a variability detection statistic that is robust against individual outlier measurements (similar to those caused by cosmic ray hits).

We perform Monte-Carlo modeling to characterize the performance of various variability-detection statistics in the presence of photometric outliers. First, we model $i = 1 \dots 10000$ light curves each containing N points randomly distributed in time. At each point in the model light curve we assigned a brightness value drawn from the Gaussian distribution characterized by the variance e^2 . In addition, 1% of the points get a “cosmic ray hit” modeled by the additional increase in brightness by a value drawn from a uniform distribution between 0 and $100e$. We, then, compute the median value, $I^{\text{non-var}}$ and the standard deviation $\sigma(I^{\text{non-var}})$ scaled from the median absolute deviation of $I^{\text{non-var}}$ values for each of the tested variability indices:

$$\sigma(I^{\text{non-var}}) = 1.4826 \times \text{median}(|I_i^{\text{non-var}} - \text{median}(I_i^{\text{non-var}})|).$$

After that, we add to each light curve an aperiodic variation characterized by a power-law power spectral density with a slope of -1 and amplitude e (equal to the noise level). We use these lightcurves to compute the median value of the variability index:

$$I^{\text{var}} = \text{median}(I_i^{\text{var}})$$

and the typical Signal-to-Noise ratio, SNR, of variability detection (among all the realizations of the noise and variability patterns):

$$\text{SNR} = (I^{\text{var}} - I^{\text{non-var}}) / \sigma(I^{\text{non-var}}).$$

The resulting values of SNR as a function of N are presented in Figure A1 for the three variability indices: the standard deviation σ , the median absolute deviation (MAD) that characterize the scatter of measurements in a light curve and the $1/\eta$ that quantifies the smoothness of a lightcurve.

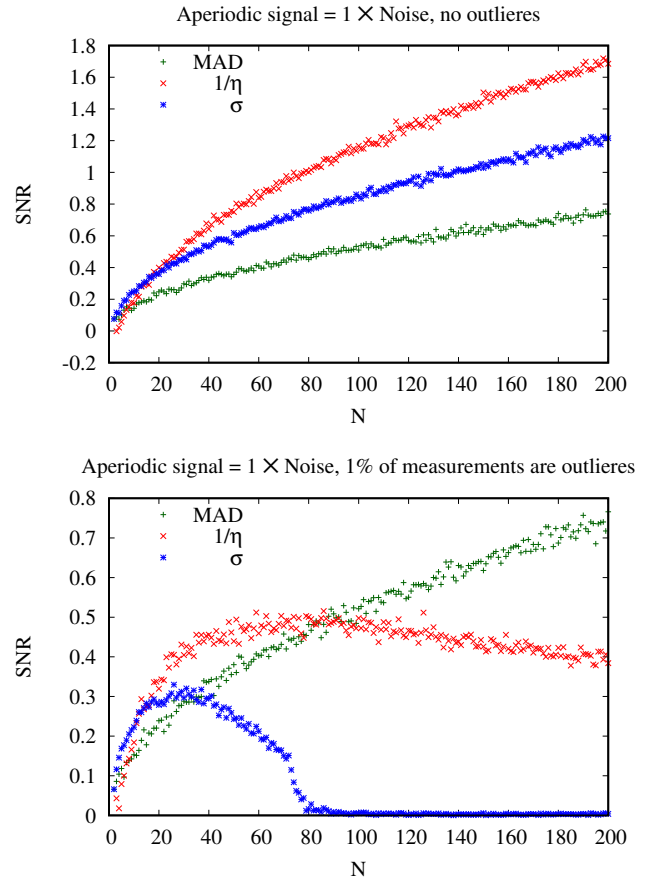


Figure A1. The simulated median signal to noise ratio of variability detection as a function of the number of light curve points with no outlier measurements (top panel) and in the presence of outliers (bottom panel).

A detailed discussion of these variability indicators can be found in Sokolovsky et al. (2017b).

Figure A1 highlights that in the absence of outlier measurements (i.e. non-periodic variability is being detected over a pure Gaussian noise) σ and $1/\eta$ typically provide a higher SNR detection for a given number of light curve points than MAD. If outlier measurements are present in light curves, they dramatically affect the efficiency of σ as a variability indicator rendering it useless as soon as each light curve has so many points that it is likely to contain at least one outlier (recall, that in our model the variability amplitude is lower than the amplitude of outliers). The ability of $1/\eta$ to identify smooth variability is also reduced considerably by outliers, while MAD maintains the SNR that is steadily increasing with N .

The simulations described above confirm that MAD may serve as a variability indicator resistant to individual outlier measurements. It is also apparent that σ is on average a more sensitive variability indicator than MAD as long as N is sufficiently low that each individual lightcurve is unlikely to contain even one outlier. However, if outliers are present in the data set, the light curves that contain outliers will predominantly be selected with σ as candidate variables. The use of MAD is still preferred to select a clean

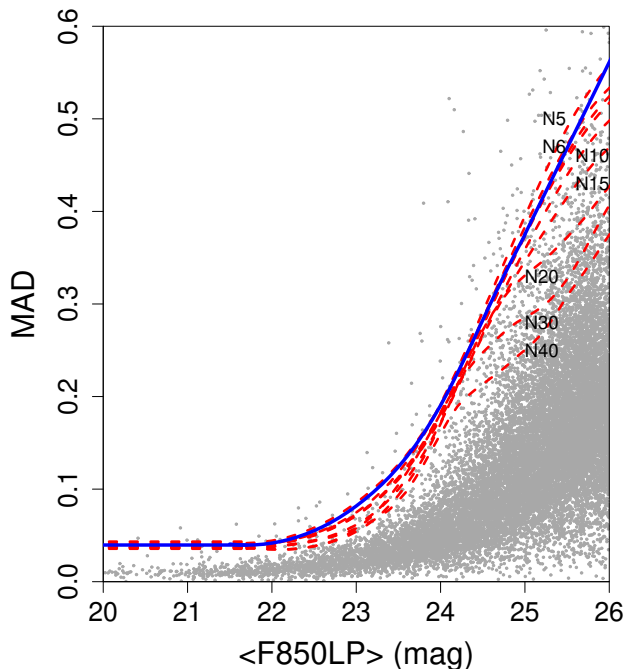


Figure A2. MAD as a function of magnitude of all sources in our initial sample. The blue solid line represents the adopted variability threshold of 3.5σ , while the red dashed lines represent the thresholds for the median under-sampled sets for different number of data points in the light curves, N .

sample of variable objects, even at the cost of a slightly lower detection efficiency compared to σ .

A2 Variability threshold dependence on the number of data points in light curves

In order to test if the 3.5σ threshold will be at a different level if we consider only light curves with a specific number of data points, we used simulations and checked if the thresholds derived from under-sampled data is lower than the adopted threshold in this work. If this is the case, then the sample of variable sources derived from applying the same threshold to all light curves (irrespective of the number of points in them) will not be affected.

We simulated ten sets of under-sampled data with the sets differing in the number of data points in the light curves ($N=5, 6, 7, 8, 9, 10, 15, 20, 30$ & 40). The number of sources of the under-sampled data are 21022, 19346, 17428, 15891, 14207, 13128, 6790, 3677, 1769 & 1350, respectively. For each set, we performed 1000 iterations and at each time, we randomly selected N data points for all the sources of our initial sample. We then calculated the MAD values and followed the procedure described in Section 3.1 to find the 3.5σ thresholds. We took the median values of the thresholds with N data points in the light curve and we compared the results with different N . In Figure A2, we plot the MAD as a function of magnitude for all the sources of our sample and the 3.5σ threshold adopted in this work (solid blue line). We over-plot the median values of 3.5σ thresholds for

Table B1. Catalogue of confirmed SNe identified in our survey.

ID	RA (J2000)	Dec (J2000)	N_p	T_{bas} (years)	$\langle F850LP \rangle$ (mag)	MAD* (σ)
7343	53.07570	-27.73630	8	0.14	24.10	11.1
9581	53.10564	-27.75084	17	2.51	22.71	4.72
14446	53.15638	-27.77966	6	0.18	24.97	4.20

different number of data points in the light curve, N (dashed black lines).

We find no extreme differences between the thresholds derived from different N . From the bright end of the magnitude distribution up to ~ 24 mag, the thresholds follow the same trend with small scatter with each other. Above ~ 24 mag, the scheme changes as the simulated thresholds are getting lower for increasing N . The adopted threshold in this work is above all the simulated ones but the set with $N=5$ above 24 mag that has slightly higher values. As long as the number of sources that have only five data points in their light curves is small, and the differences in the thresholds is not significant, we expect no false variability induced by the different number of data points in the light curves.

APPENDIX B: OBSERVATIONAL PROPERTIES AND LIGHT CURVES OF SUPERNOVAE

Table B1 lists the observational properties, while Figure B1 presents our photometry of the identified SNe. All three SNe have been reported previously in the literature (Strolger et al. 2004; Riess et al. 2007).

This paper has been typeset from a $\text{T}_{\text{E}}\text{X}/\text{L}^{\text{A}}\text{T}_{\text{E}}\text{X}$ file prepared by the author.

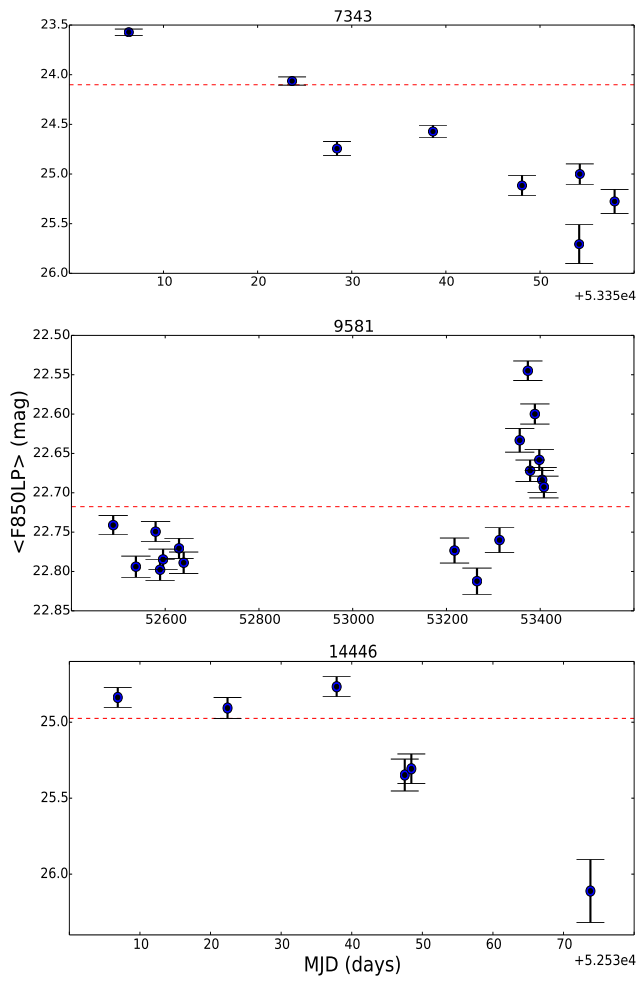


Figure B1. Light curves of the confirmed SNe identified in this study. The dashed line indicates the median magnitude and the number on the top of each plot indicates the identifier of the source.